Joint gas and stellar dynamical models of WLM: an isolated dwarf galaxy within a cored, prolate DM halo

Gigi Y. C. Leung [1], Ryan Leaman [1]★, Giuseppina Battaglia,[2,3] Glenn van de Ven [4], Alyson M. Brooks,[5] Jorge Peñarrubia[6] and Kim A. Venn[7]

[1]*Max-Planck Institut für Astronomie, Königstuhl 17, D-69117 Heidelberg, Germany*
[2]*Instituto de Astrofísica de Canarias, Calle Vía Láctea s/n, E-38205 La Laguna, Tenerife, Spain*
[3]*Departamento de Astrofísica, Universidad de La Laguna, E-38200 La Laguna, Tenerife, Spain*
[4]*Department of Astrophysics, University of Vienna, Türkenschanzstrasse 17, A-1180 Vienna, Austria*
[5]*Department of Physics and Astronomy, Rutgers, The State University of New Jersey, 136 Frelinghuysen Road, Piscataway, NJ 08854, USA*
[6]*Institute for Astronomy, University of Edinburgh, Royal Observatory, Blackford Hill, Edinburgh EH9 3HJ, UK*
[7]*Department of Physics and Astronomy, University of Victoria, Victoria, BC V8W 3P2, Canada*

ABSTRACT

We present multitracer dynamical models of the low-mass ($M_* \sim 10^7$), isolated dwarf irregular galaxy WLM in order to simultaneously constrain the inner slope of the dark matter (DM) halo density profile (γ) and flattening (q_{DM}), and the stellar orbital anisotropy (β_z, β_r). For the first time, we show how jointly constraining the mass distribution from the H I gas rotation curve and solving the Jeans equations with discrete stellar kinematics lead to a factor of ~ 2 reduction in the uncertainties on γ. The mass-anisotropy degeneracy is also partially broken, leading to reductions on uncertainty by ~ 30 per cent on M_{vir} (and ~ 70 per cent at the half-light radius) and ~ 25 per cent on anisotropy. Our inferred value of $\gamma = 0.3 \pm 0.1$ is robust to the halo geometry, and in excellent agreement with predictions of stellar feedback-driven DM core creation. The derived prolate geometry of the DM halo with $q_{DM} = 2 \pm 1$ is consistent with Lambda cold dark matter simulations of dwarf galaxy haloes. While self-interacting DM (SIDM) models with $\sigma/m_X \sim 0.6$ can reproduce this cored DM profile, the interaction events may sphericalize the halo. The simultaneously cored and prolate DM halo may therefore present a challenge for SIDM. Finally, we find that the radial profile of stellar anisotropy in WLM (β_r) follows a nearly identical trend of increasing tangential anisotropy to the classical dwarf spheroidals, Fornax and Sculptor. Given WLM's orbital history, this result may call into question whether such anisotropy is a consequence of tidal stripping in only one pericentric passage or if it instead is a feature of the largely self-similar formation and evolutionary pathways for some dwarf galaxies.

Key words: galaxies: kinematics and dynamics – galaxies: dwarf.

1 INTRODUCTION

The shape and radial density profile of dark matter (DM) haloes provides a window into the nature of DM, and the efficiency of baryonic feedback processes that influence the galaxies residing in these haloes (e.g. Di Cintio et al. 2014). For instance, DM-only cosmological and *N*-body simulations have shown that, under the Lambda cold dark matter (ΛCDM) cosmological framework, the DM haloes around galaxies follow a cuspy density profile characterized by an NFW profile (e.g. Navarro, Frenk & White 1996b; Dutton & Macciò 2014). Hydrodynamic simulations that incorporate baryonic feedback from stars and active galactic nucleus find that not only are the star formation properties altered, but also the repeated ejection of gas from central regions of low-mass galaxies can result in a reduction of the inner cumulative baryonic and dark mass distribution (e.g. Navarro, Eke & Frenk 1996a; Read & Gilmore 2005; Mashchenko, Couchman & Wadsley 2006; Peñarrubia et al. 2012; Pontzen & Governato 2012).

The DM halo properties may hence be correlated with the baryonic content of the galaxies. For example, Di Cintio et al. (2014) show that the inner slope of the DM haloes correlates with the stellar-mass-to-halo-mass ratio in their simulated galaxies, and Read, Agertz & Collins (2016) showed with hydrodynamical simulations that the core size of the DM haloes in dwarf galaxies generally correlates with the half-light radii of the stellar component. Significant variation in the predicted range of DM fractions (in terms of mass with respect to the total mass of the galaxy) is seen either directly from cosmological zoom-in simulations (Brook 2015) or from abundance matching predictions (e.g. Leauthaud et al. 2012; Sawala et al. 2013). Understanding this stochasticity is therefore crucial to gain a better understanding of the efficiency with which baryonic feedback can suppress star formation – and simultaneously alter the initial DM halo profiles.

Being the most DM-dominated objects in the Universe, dwarf galaxies act as prime laboratories for testing the impact of baryonic feedback and the nature of DM. Various techniques have been adopted to infer the relative contribution of stellar and dark components in low-mass galaxies. For example, the decomposition

★ E-mail: ryan.c.leaman@gmail.com

of rotation curves obtained from H I kinematics has been used to study the fractional amount of DM in low-mass galaxies (e.g. Lelli, Fraternali & Sancisi 2010; Swaters et al. 2011; Adams et al. 2014; Katz et al. 2017). These results typically found that despite the uncertainties in stellar-mass-to-light ratios, the baryonic mass was a small fraction of that necessary to reproduce the circular velocity profiles. These objects thus can provide a stringent test also on the nature of DM and/or non-Newtonian dynamics (e.g. Lelli et al. 2010; McGaugh & Milgrom 2013; Vogelsberger et al. 2014).

Many of these same studies found that that the rotation curves of nearby dwarf galaxies have inner density or cumulative mass profiles that are shallower/smaller than the cosmologically predicted cuspy NFW profile of DM-only simulations (e.g. Oh et al. 2011; Adams et al. 2014; Brook 2015). This instead may be a signature of the aforementioned stellar feedback-driven DM coring, which is likely to be most effective in low-mass galaxies with shallow potentials, but still significant star formation (Read & Gilmore 2005; Di Cintio et al. 2014). A challenge in assessing this scenario is that the asymptotic slope of the DM density profile is difficult to infer and depends on the particular mass profile assumed. Several studies instead have characterized the density profile slope at a fixed physical scale, or fraction of the virial radius or stellar half-light radius (e.g. Hague & Wilkinson 2013; Li et al. 2019; Read, Walker & Steger 2019). The need for isolated galaxies that have not been environmentally stripped of gas, and of a high enough mass such that the H I rotation is measurable, means that these techniques have not typically been used for the most nearby Local Group or low-mass satellite galaxies of the Milky Way (MW).

In those systems, stellar kinematics are predominantly used to measure the DM density profiles (either estimating an asymptotic slope or the slope of the profile at fixed radius), through the virial mass estimates (Walker & Peñarrubia 2011), the Jeans equations (e.g. Łokas 2009; Zhu et al. 2016), or Schwarzschild models (e.g. Breddels et al. 2013; Kowalczyk et al. 2018). Measuring the mass profile from stellar kinematics suffers from uncertainties associated with the unknown velocity anisotropy, known as the mass-anisotropy degeneracy. To break the mass-anisotropy degeneracy, the higher order moment (kurtosis) has been have utilized (e.g. Łokas 2009; Breddels & Helmi 2013). As this degeneracy is found to have a spatial dependence and is minimal at the half-light radius (e.g. Wolf 2010; Errani, Peñarrubia & Walker 2018), other authors have separated stellar kinematics into populations of different chemistry with different spatial and kinematical distributions to serve as a lever arm to understand the host potential (Battaglia et al. 2008; Walker & Peñarrubia 2011; Zhu et al. 2016). The constraints on the inner slopes of the DM density profiles by stellar kinematics alone are difficult however. For example, while Walker & Peñarrubia (2011) can exclude a completely cuspy NFW profile in the DM halo of Fornax with up to 96 per cent significance, the estimated inner slope of $\gamma = 0.5 \pm 0.4$ (where γ parametrizes the inner slope of a generalized NFW (gNFW) profile, with $\gamma = 0$ corresponding to a cored profile and $\gamma = 1$ an NFW profile) still has a large uncertainty. Similarly, even with a discrete Jeans model on two chemically distinct populations, Zhu et al. (2016) could only constrain the inner slope of the DM halo of Sculptor to be within $\gamma = 0.5 \pm 0.3$. In another study, Kowalczyk et al. (2018) showed that while a cored profile is preferred by their models for Fornax, cuspy NFW and Einasto profiles fall within the 1σ uncertainties. Using orbit-based dynamical models extending also to higher moments, Breddels & Helmi (2013) found that the stellar kinematics of four dwarf spheroidals (dSphs) Fornax, Sculptor, Carina, and Sextans are compatible with both cuspy and cored DM haloes. Given the difficulties in robustly inferring

the profile shape through single or even multiple population stellar tracers, it is desirable to study low-mass dwarf galaxies with multiple kinematic tracers (e.g. gas and stars) with new analysis methods.

Combining a collisional gas tracer with discrete kinematic stellar tracers in principle should offer a more robust characterization of the host potential. Despite their different orbital structure, the gas and the stellar kinematics should consistently trace the same potential when all sources of orbital energy are accounted for. Combining observations of stars and gas kinematics in the same galaxy then offers a way to break the mass-anisotropy degeneracy and better characterize the DM halo properties. Also, while stellar kinematics typically only allows for fitting the mass enclosed within the stellar radii of the chemodynamical components, cold gas provides kinematic information over a much larger radial range. Observations of gas and stars in homogenous observations of a variety of galaxies were presented in Leung et al. (2018) and for $8.5 < \log L_\star < 9.5$ dwarf galaxies in Adams et al. (2014). However, neither of these studies leveraged the tracers simultaneously to measure halo properties from the combined information of both tracers. Nevertheless, there appears great promise in exploiting the simultaneous tracers for galaxies where both exist.

Apart from constraints on the underlying gravitational potential, proper modelling of the stellar kinematics can recover their orbit distribution in the galaxy. The shape of the velocity ellipsoid, often parametrized in terms of an anisotropy parameter such as $\beta_\phi = 1 - (\sigma_\phi/\sigma_R)^2$ (where σ_ϕ and σ_R are the velocity dispersions along the azimuthal and radial direction, respectively, in a cylindrical coordinates), provides an understanding of the relative amount of random motions in the tangential and radial directions. These quantities may be intimately tied to the formation and evolutionary pathways of the dwarf galaxies – either environmental or secular. Characterizing the anisotropy profiles of dwarfs in the Local group is particularly helpful in understanding any evolutionary connection between dwarf irregulars (dIrrs) and dSphs.

For example, predictions of simple dissipationless collapse result in an isotropic core surrounded by an envelope of more radial orbits (van Albada 1982). However, dwarfs with sufficiently radially anisotropic orbits may have undergone bar formation, which after subsequent buckling and excitation of bending modes can result in significant morphological transformations (e.g. Raha et al. 1991; Mayer et al. 2006). Tidally stripped galaxies are thought to have strongly tangential anisotropy in their outer regions as the radial orbits with larger apocentres may be preferentially removed (Klimentowski et al. 2009).

The tangential velocity anisotropies found in dSphs (e.g. Zhu et al. 2016; Kowalczyk et al. 2018) may agree with some tidal transformation scenarios (e.g. Klimentowski et al. 2009), where dIrrs are tidally disturbed and lose their gas and form dSphs, leaving behind a tangential stellar anisotropy distribution for the resultant dSph. This scenario, however, may be challenged by the existence of transition-type dwarfs in isolation (e.g. VV124; Vorontsov-Velyaminov 1959), and the suggested similarities in the ratio of ordered to random motion V/σ between dSphs and dIrrs (Wheeler et al. 2017). Comparable estimates of velocity anisotropy in isolated dwarf galaxies, yet to be determined, would serve as a crucial control sample, and help differentiate if this signature is caused by environmental effects or rather something intrinsic to the formation of any low-mass dwarf.

The recovery of the stellar anisotropy is not trivial and several degeneracies work to prevent accurate understanding of the stellar orbital or DM halo properties. In addition to the aforementioned mass-anisotropy degeneracy, Binney & Tremaine (1987) have shown that the derived anisotropy is highly degenerate with the DM halo geom-

etry. This then means that another parameter, the halo flattening q_{DM}, needs to be introduced in dynamical models in order to recover an unbiased estimate of β. In a handful of MW-mass galaxies, inference of the DM halo flattening has been produced from H I gas kinematics and structure (e.g. O'Brien, Freeman & van der Kruit 2010; Khoperskov et al. 2014; Peters et al. 2017b), with the results depending on the viewing angle and configuration (edge-on, polar ring) as well as assumptions on the gas opacity. For low-mass nearby galaxies, while attempts in dynamical modelling incorporating a halo flattening with fixed anisotropy have been attempted (e.g. Hayashi & Chiba 2012), incorporating variable DM profiles (γ, q_{DM}) and anisotropy simultaneously has not been done as the constraints on parameters of interest get understandably poorer with the increasing (but necessary) model complexity. The necessity of understanding DM in low-mass dwarfs, breaking anisotropy and halo property degeneracies, and testing the intrinsic orbit structure of *isolated* dwarf galaxies clearly motivates the need for new analysis techniques and observations.

In this work, we demonstrate a promising way forward, by jointly modelling the stellar and gaseous kinematics in dwarf galaxies that have both resolved stellar kinematics and well-behaved H I gas rotation curves. With an alternate constraint on the galaxy's potential from the gas rotation curve, the stellar anisotropy estimate should be improved. A second necessary aspect of the modelling is to flexibly parametrize the DM halo's shape and inner density profile slope.

Often, the nature of the dwarf galaxies prevents observable stellar and gaseous tracers from co-existing, such as in the case of the nearby quenched dSphs, or the low-gas fraction transition dwarfs, or increases the observational cost of getting stellar kinematics in gas-rich distant dIrrs. In the few dwarfs where both resolved stellar and gaseous kinematics have been observed (Leaman et al. 2012; Kirby et al. 2014), the dynamical mass estimates from both tracers individually show agreement – provided that contributions of non-circular motions are taken into account (e.g. Hinz, Rix & Bernstein 2001; Read & Steger 2017), a joint dynamical model leveraging both tracers simultaneously has, however, not yet been attempted.

One of the prime targets, which is near enough for obtaining sufficient stellar kinematics and massive enough to have a well-defined gaseous rotation curve, is the isolated dIrr Wolf–Lundmark–Melotte (WLM; Wolf 1910; Melotte 1926). WLM lies at a distance of ∼1 Mpc from both the Milky Way and M31. The distance between WLM and its nearest neighbour, a low-mass dSph Cetus (enclosed mass at half-light radius of $M \sim 4 \times 10^7 \, M_\odot$; Kirby et al. 2014), is ∼250 kpc (Whiting, Hau & Irwin 1999). With a velocity of $v_{LG} \sim -32 \, km \, s^{-1}$ towards the barycentre of the Local Group, Leaman et al. (2012) suggested that WLM has just passed its apocentre and would have at most one pericentre passage in its lifetime, which occurred at least 11 Gyr ago. Constructing our proposed dynamical model of a dwarf galaxy in such extreme isolation would provide a null test on the effects of external influences, such as tides and ram pressure, and provide one of the most detailed views of the DM halo and orbit structure of a low-mass dwarf. Also, WLM's isolated location (together with its comprehensive constraints on thickness, stellar dispersion, and circular velocity) renders it as an excellent test case for modified gravity, as external field effects cannot be invoked.

In the following, we first describe our H I and stellar data in Section 2. We then lay out the observational and model ingredients including our construction of the dynamical model, the spatial distribution of the kinematic tracers, the baryonic and DM density profile, and the steps of our parameter estimation in Section 3. We present the obtained DM halo parameters and velocity anisotropies of WLM in Section 4. In Section 5, we discuss the cosmological implications of the derived DM halo profile and flattening, as well as
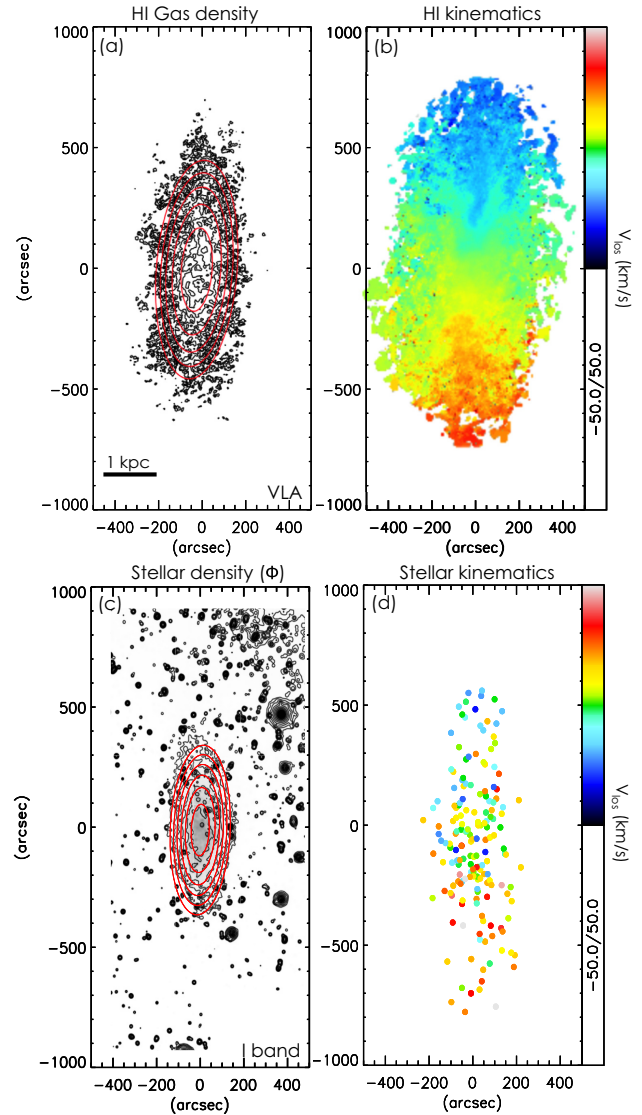

Figure 1. Photometric and kinematic data. (a) and (b): H I surface density and velocity maps (Iorio et al. 2017). (c): Greyscale and black contours are the smoothed *I*-band image of WLM. The fitted MGEs are overlaid in red. (d) Discrete velocity measurements.

the meaning of the derived orbital structure in terms of the evolution of dwarf galaxies. We conclude in Section 6.

2 DATA

2.1 H I interferometric data

We have taken the H I integrated intensity map and the circular velocity V_c estimated using H I kinematics originally presented in Kepley et al. (2007) and re-analysed by Iorio et al. (2017). The interferometric data are taken using the Very Large Array, with a beam size of ∼10 arcsec and a velocity resolution of ∼2.6 km s^{-1}. The integrated intensity map is shown as black contours on the left-hand panel of Fig. 1, and the velocity map from which the circular velocities are derived from is shown on the right-hand panel of Fig. 1. From the velocity map, Iorio et al. (2017) have derived an inclination of 74° and a position angle of 174°, which we adopt throughout the whole paper. Their derived V_c is shown in Fig. 2.
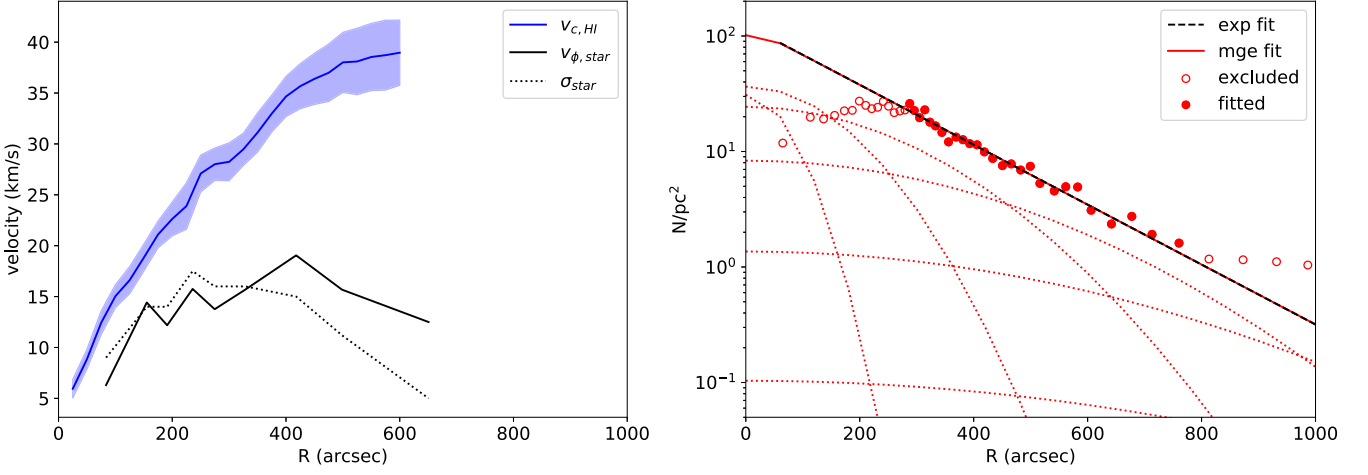
Figure 2. Left: H I Circular velocities derived by Iorio et al. (2017) with the velocity map shown in Fig. 1(b) in blue, with 1σ uncertainties shown by the light blue band. The binned stellar mean velocity ($v_{\phi,\,\text{star}}$) and velocity dispersion (σ_{star}) profiles are shown in solid and dotted black lines, respectively. Right: The RGB star counts are shown as red circles, with the open circles indicating points that are excluded due to crowding and background contamination in the fitting of exponential profile as adopted in Leaman et al. (2013). The fitted exponential profile is shown in the black dashed line. The individual MGEs fitted to the exponential profile are shown in red dotted lines and the total MGE is shown in a red solid line.

2.2 Photometric data

The *I*-band photometry was obtained using the INT Wide Field Camera and presented initially in McConnachie et al. (2005) and covers a 36 arcmin × 36 arcmin field of view. We used the resolved radial stellar number density profiles constructed from these data and presented in Leaman et al. (2012) in both *I* band and the *JHK* photometric observations of Tatton, Cioni & Irwin (2011). We refer the reader to Leaman et al. (2012) for details of the profile construction.

In addition, we utilize photometric observations in the *I* band taken with the MOSAIC-II imager formerly installed on the 4-m Blanco telescope at CTIO. These observations were taken in excellent seeing conditions (∼0.8 arcsec) on 2009 September 11–12 (PI: Leaman 2009B-0337). The CCD has a pixel scale of 0.27 arcsec per pixel and the images were processed and coadded through the NOAO Science Archive pipelines. The co-added stacked image that was used to build the stellar contribution to the mass distribution covers a field of view of 0.63 × 0.67 deg. Further details of the observations and reductions will be presented in Hughes et al. (in preparation).

2.3 Resolved stellar spectroscopy

We utilize a discrete set of line-of-sight velocity measurements from 180 member giant branch stars obtained using FORS2 on VLT and DEIMOS on Keck. The typical uncertainties on velocity are $\delta V \sim$ 6–9 km s^{-1}, and the reader is referred to Leaman et al. (2009, 2012, 2013) for details on the data reduction and observations. This sample has already been cleaned from non-member contaminants on the basis of line-of-sight velocity and position metrics. The position and line-of-sight velocities of the stellar kinematic members are plotted in Fig. 1(e).

3 DISCRETE JEANS MODEL

Given a total gravitational potential Φ, a velocity anisotropy and an inclination, the Jeans equations (Jeans 1922) specify the projected second velocity moment $V_{\text{RMS}}^2 = V_{\text{mean}}^2 + \sigma^2$ of a kinematic tracer of known density, where V_{mean} and σ are the line-of-sight mean

velocity and velocity dispersion, respectively. To begin, we assume axisymmetry for WLM and utilize Jeans Axisymmetric Models (JAMs; Cappellari 2008) to solve for the predicted velocity moments. The Jeans equations, under the axisymmetric assumptions, can be written as

$$\frac{\partial (R\nu\overline{v_R^2})}{\partial R} + R\frac{\partial (\nu\overline{v_R v_z})}{\partial z} - \nu\overline{v_\phi^2} + R\nu\frac{\partial \Phi}{\partial R} = 0,$$

$$\frac{\partial (R\nu\overline{v_R v_z})}{\partial R} + R\frac{\partial (\nu\overline{v_z^2})}{\partial z} + R\nu\frac{\partial \Phi}{\partial z} = 0,$$

$$\nu\overline{v_\phi^2}(R, z) = \left(1 - \frac{1}{\beta_z}\right)\left[R\frac{\partial}{\partial R}\left(\int_z^\infty \nu\frac{\partial \Phi}{\partial z}dz\right)\right.$$

$$\left. + \int_z^\infty \nu\frac{\partial \Phi}{\partial z}dz\right] + R\nu\frac{\partial \Phi}{\partial R}, \quad (1)$$

where $\nu(R, z)$ is the surface density of the kinematic tracer and $\Phi(R, z)$ is the axisymmetric gravitational potential. Again, (v_R, v_z, v_ϕ) are the velocity components in the three dimensions of the cylindrical coordinates (R, z, ϕ), with $\beta_z = 1 - \overline{v_z^2}/\overline{v_R^2}$ being a velocity anisotropy. Following Cappellari (2008), the velocity ellipsoid is assumed to be aligned with the cylindrical coordinates such that $\overline{v_R v_z} = 0$.

3.1 Constructing the potential

We construct the gravitational potential Φ with three components, namely the gaseous component, the stellar component, and the DM component. Each of the components is parametrized by a set of Multi-Gaussian Expansions (MGEs; Emsellem, Monnet & Bacon 1994), which deproject and decompose 2D surface densities into superpositions of 3D Gaussian components, as is required for our Jeans model. The 2D (projected) surface densities $\Sigma(x', y')$ are first decomposed into Gaussians:

$$\Sigma(x', y') = \sum_{k=1}^N I_{0,k} \exp\left[-\frac{1}{2\sigma_k^2}\left(x'^2 + \frac{y'^2}{q_k'^2}\right)\right], \quad (2)$$

where $I_{0,k}$ is the central density, σ_k is the width, and q_k' is the observed flattening of each of the Gaussian components k. The 2D Gaussian

Table 1. MGEs of the gaseous component obtained from H I surface density map.

$I_{0,\,\rm gas}$ ($\rm M_\odot\,pc^{-2}$)	$\sigma_{\rm gas}$ (arcsec)	$q_{\rm gas}$
3.775	40.58	0.28
1.854	91.71	0.30

Table 2. MGE of the smoothed *I*-band stellar surface brightness profiles used to constrain the stellar mass distribution, normalized to a total stellar mass of $M_\star = 1.1 \times 10^7\,\rm M_\odot$.

$I_{0,\,\star}$ ($\rm M_\odot\,pc^{-2}$)	$\sigma_\star$ (arcsec)	$q_\star$
2.750	14.74	0.50
14.72	130.8	0.41
6.239	199.0	0.42

components are then deprojected to describe the 3D density $\nu(R, z)$:

$$\nu(R, z) = \sum_{k=1}^{N} I_{0,k} \exp\left[-\frac{1}{2\sigma_k^2}\left(R^2 + \frac{z^2}{q_k^2}\right)\right], \tag{3}$$

with $q_k = \sqrt{(q_k'^2 - \cos^2 i)}/\sin i$ describing the intrinsic flattening of each component deprojected given an inclination i. For all the components, we adopt the same PA and inclination as the ones derived from the H I velocity map (PA = 174° and $i = 74°$). Below we provide details on the distributions of the various components.

3.1.1 Gaseous component

We fit MGEs to the H I integrated intensity map using the PYTHON code provided by Cappellari (2008). When fitting the MGEs, we fixed the inclination to be 74°, consistent with the derived inclination from the H I velocity field by Iorio et al. (2017). Fig. 1 shows the best-fitting MGEs in red contours overlaid on the H I gas density contours. We normalized the MGEs to the total neutral gas mass of WLM, $1.1 \times 10^8\,\rm M_\odot$, which is taken from the single dish observations of Hunter et al. (2011). We apply a correction factor of 1.4 to account for the presence of Helium; this yields a total gas mass of $M_{\rm gas,tot} \sim 1.54 \times 10^8\,\rm M_\odot$. The resultant gaseous MGE parameters, the peak surface density $I_{0,\,\rm gas}$, the width $\sigma_{\rm gas}$, and flattening $q_{\rm gas}$, of each of the constituent Gaussians are presented in Table 1. The flattening parameter q is given by the ratio between the short and long axis of each Gaussian.

3.1.2 Stellar component

To obtain a smooth stellar distribution, we utilize the *I*-band photometry that traces evolved stars and avoids the irregular light density profiles of bluer bands caused by the often patchy distribution of young stars. We first smooth the *I*-band image with a Gaussian of width 5 arcsec in order to remove the stochasticity inherent in the nearby resolved systems, and then fit MGEs to the smoothed projected surface density map. The MGEs are then normalized to a total stellar mass. The fitted MGEs are overlaid on top of the *I*-band image in Fig. 1(c). The resultant stellar MGE parameters $I_{0,\,\star}$, $\sigma_\star$, and $q_\star$, as normalized to $M_\star = 1.1 \times 10^7\,\rm M_\odot$ (Jackson et al. 2007), are presented in Table 2. Despite the presence of some foreground stars in the image, we find that their presence does not change the MGE fits.

Table 3. MGE of the RGB star counts fitted by an exponential profile to measurements within 279–813 arcsec to avoid bias caused by crowding, normalized to a total stellar mass of $M_\star = 1.1 \times 10^7\,\rm M_\odot$. Note that since the MGEs are fitted from one-dimensional star-count profiles, we take the outermost $q_\star$ as fitted from the *I*-band image (Table 2) as the $q_\star$ for all the MGEs here.

$I_{0,\,\star}$ ($\rm M_\odot\,pc^{-2}$)	$\sigma_\star$ (arcsec)	$q_\star$
1.601	64.769	0.422
1.882	135.675	0.422
1.259	232.891	0.422
0.430	348.873	0.422
7.029×10^{-2}	476.647	0.422
5.344×10^{-3}	611.309	0.422
1.893×10^{-4}	749.823	0.422
2.986×10^{-6}	893.630	0.422
1.233×10^{-8}	1057.583	0.422

3.1.3 DM component

To model the DM contribution to the potential of WLM, we utilize a gNFW (Zhao 1996) profile to describe our DM halo. This has a radial density profile of

$$\rho(R) = \frac{\rho_{\rm s}}{(R/r_{\rm s})^\gamma (1 + R/r_{\rm s})^{3-\gamma}}, \tag{4}$$

with $\rho_{\rm s}$, $r_{\rm s}$, and γ being the scale density, scale radius, and slope of the DM profile, respectively. To test the influence and degeneracy of non-spherical mass distributions, we also allow the DM halo to be axisymmetric with a flattening $q_{\rm DM}$ (with $q_{\rm DM} = c/a$, where c and a are the axes of the DM halo, perpendicular and parallel to the axis of symmetry, respectively, and the transformation from Cartesian coordinate to R in equation 4 is $R = \sqrt{x^2 + y^2 + (z/q_{\rm DM})^2}$). We normalize our DM haloes with the circular velocities at $r_{\rm s}$ such that DM haloes with the same ($r_{\rm s}$, γ, $\rho_{\rm s}$) but different $q_{\rm DM}$ would have the same $V_{\rm c}(r_{\rm s})$. This normalization is done so that the parameter $q_{\rm DM}$ is only sensitive to the shape of the DM halo but not the overall enclosed mass. A DM halo parametrized by a particular set of ($r_{\rm s}$, γ, $\rho_{\rm s}$ and $q_{\rm DM}$) can then be decomposed into MGEs – which, together with the gaseous and stellar MGEs, provides a representation of the total gravitational potential of WLM.

3.2 Surface density of the kinematic tracer

To obtain the density profile of the kinematic tracer ν, we utilize the discrete giant branch star counts from Leaman et al. (2012). These star counts are constructed from photometric catalogues that have had a comparable colour and magnitude selection to the spectroscopic sample – thus providing the most representative density distribution for the kinematic tracer population. The stellar density profile for the kinematic tracers is shown in the right-hand panel of Fig. 2 in red circles. The inner flattened number count profile is potentially caused by crowding and we correct for it by fitting first an exponential profile to the star counts beyond the crowded region ($\gtrsim 300$ arcsec), as shown in the black line. We then fit MGEs to the black dashed line and we again adopt the same PA and inclination (PA = 174° and $i = 74°$). The resultant MGE fit is shown by the red solid line and the MGE parameters are listed in Table 3. These MGEs are adopted as the surface density of the kinematic tracer in our models throughout the rest of the paper. Readers interested in how robust our results are with respect to the choice of different profiles can refer to Appendix A, where we show the impact of this incompleteness correction on our final results.

3.3 Model parameters

The relevant velocity anisotropy for the JAM model is $\beta_z = 1 - \overline{v_z^2}/\overline{v_R^2}$, where $\overline{v_z^2}$ and $\overline{v_R^2}$ are the second velocity moments along the z and R axes, respectively, of the cylindrical coordinate system.[1]

Typically, the modelled $V_{\mathrm{RMS}}^{\mathrm{mod}}$ can be compared directly with the observed $V_{\mathrm{RMS}}^{\mathrm{obs}}$ for spatially binned data. In the case of nearby dwarf galaxies, spherical Jeans models have often been applied on the observed σ (assuming that rotation is negligible) in spatial bins along the major axis of the galaxy (e.g. Battaglia et al. 2011). However, for fully axisymmetric models, it is more flexible to fit to the discrete stellar kinematic data directly. To do this, we compare the observed line-of-sight velocity $V_{\mathrm{LOS},i}$ of each star $i \in N$, where N is the total number of observed stars, to the probability distribution function of the model line-of-sight velocity $V_{\mathrm{LOS,mod}}$ at their projected location on the sky plane (x_i, y_i). The discrete data are by construction, only providing a single V_{LOS} value, while the relative contributions of $V_{\mathrm{mean}}^{\mathrm{mod}}$ and σ^{mod} to $V_{\mathrm{RMS}}^{\mathrm{mod}}$ are not constrained by the Jeans model itself. We therefore follow Satoh (1980) and Cappellari (2008) and introduce κ as another free parameter to characterize the amount of rotation the system has relative to an *isotropic rotator*, where $\kappa = \overline{v_\phi}/\sqrt{\overline{v_\phi^2} - \overline{v_R^2}}$. As described in Cappellari (2008), $\kappa = 1$ is a rotating system with a symmetric velocity ellipsoid in the R–ϕ plane (and spherically isotropic in cases where $\sigma_z = \sigma_R$), while κ approaches 0 when the system angular momentum drops, or the anisotropy increases. While not a direct analogue for angular momentum, the parametrization allows for a flexible way to fit the discrete velocity field. Readers interested in the mathematical procedures with which κ decomposes $V_{\mathrm{RMS}}^{\mathrm{mod}}$ into $V_{\mathrm{mean}}^{\mathrm{mod}}$ and σ^{mod} components can refer to equations (35)–(38) of Cappellari (2008).

Assuming a Gaussian velocity probability distribution function, the probability of $V_{\mathrm{LOS},i}$ at the position of each star i can be written as

$$\ln P(V_{\mathrm{LOS,i}}) = \ln \frac{1}{\sqrt{2\pi\left((\delta V_{\mathrm{LOS,i}})^2 + (\sigma^{\mathrm{mod}}(x_i, y_i))^2\right)}}$$
$$- \frac{1}{2} \frac{\left(V_{\mathrm{LOS,i}} - V_{\mathrm{mean}}^{\mathrm{mod}}(x_i, y_i)\right)^2}{(\delta V_{\mathrm{LOS,i}})^2 + \left(\sigma^{\mathrm{mod}}(x_i, y_i)\right)^2}, \quad (5)$$

where $\delta V_{\mathrm{LOS,i}}$ is the error of the observed $V_{\mathrm{LOS,i}}$.

With the inclination and the position angle fixed ($i = 74°$, PA $= 174°$), the inputs for calculating the likelihood $P(V_{\mathrm{los,i}})$ through the JAM model with equation (5) are: (1) the gravitational potential Φ specified by MGEs, (2) the tracer density distribution specified by the stellar MGEs, (3) the velocity anisotropy β_z, and (4) the κ parameter. The free parameters in constructing Φ are the total stellar mass $M_{\star,\mathrm{tot}}$, q_{DM}, r_s, γ, and ρ_s. We assume that β_z^2 and κ are constant with radius. We therefore have seven model parameters: $M_{\star,\mathrm{tot}}$, $M_{\mathrm{gas,tot}}$, β_z, κ, q_{DM}, r_s, γ, and ρ_s (see Table 4).

---

[1] We note that under the assumptions of the JAM model, the vertical velocity dispersion is intrinsically coupled to the self-gravity of the disc plane, in a quasi-hydrostatic equilibrium, and thus β_z primarily reflects the vertical mass density distribution of the galaxy – however, we show later the insight that other components of the velocity ellipsoid provide on the orbital structure of WLM.

[2] We have also ran the models with the Mamon–Lokas profile and found that the fitted anisotropy profile remains constant over the radial range where we have kinematic tracers.

Table 4. The adopted priors on each of the model parameters.

Parameter	Distribution	Range
$M_\star$	normal	$1.1 \pm 0.56 \times 10^7 \, \mathrm{M_\odot}$
M_{gas}	normal	$1.54 \pm 0.77 \times 10^8 \, \mathrm{M_\odot}$
β_z	uniform	$[-2.0, 1.0]$
κ	uniform	$[0.0, 1.5]$
q_{DM}	uniform/fixed	$[0.1, 5.0]$
r_s	uniform	$[500, 10\,000]$ pc
γ	uniform	$[0.0, 1.0]$
ρ_s	uniform	$[0.001, 0.15] \, \mathrm{M_\odot \, pc^{-3}}$

3.4 MCMC sampling

To obtain marginalized distributions and covariances between the parameters of the most likely models, we sample the likelihood space using the affine-invariant MCMC ensemble sampler implemented in the python package EMCEE (Foreman-Mackey et al. 2013). We employ 200 walkers, each iterated through 300 steps; the burn-in phase is 100 steps for each walker.

We constrain $M_{\star,\mathrm{tot}}$ and $M_{\mathrm{gas,tot}}$ with their observed values $1.1 \times 10^7 \, \mathrm{M_\odot}$ and $1.54 \times 10^8 \, \mathrm{M_\odot}$, respectively, through a prior with a normal distribution of width specifying the measurement error of 50 per cent:

$$\ln Pr_1(M_{\star,\mathrm{tot}}, M_{\mathrm{gas,tot}}) = \ln \frac{1}{\sqrt{2\pi(0.5 \times 1.1 \times 10^7)^2}}$$
$$- \frac{(M_{\star,\mathrm{tot}} - 1.1 \times 10^7)^2}{2 \times (0.5 \times 1.1 \times 10^7)^2}$$
$$+ \ln \frac{1}{\sqrt{2\pi(0.5 \times 1.54 \times 10^8)^2}}$$
$$- \frac{(M_{\mathrm{gas,tot}} - 1.54 \times 10^8)^2}{2 \times (0.5 \times 1.54 \times 10^8)^2}. \quad (6)$$

For the other model parameters, we apply a uniform prior; the explored ranges of each of the parameters are listed in Table 4.

We run two sets of MCMC processes: one that only uses information from the stellar kinematics ('Stars only') and one with the observed H I V_c ($V_{c,\mathrm{HI}}$) as a constraint on the gravitational potential ('Stars + Gas'). In the case for which we include $V_{c,\mathrm{HI}}$ as a constraint on the gravitational potential, we introduce additionally a second prior term, which evaluates

$$\ln Pr_2(M_{\star,\mathrm{tot}}, q_{\mathrm{DM}}, r_s, \gamma, \rho_s) = \ln\left(\Sigma_j\left(\frac{1}{\sqrt{2\pi(\delta V_{c,\mathrm{HI}}(R_j))^2}}\right.\right.$$
$$\left.\left. - \frac{(V_{c,\Phi}(R_j) - V_{c,\mathrm{HI}}(R_j))^2}{2 \times \delta V_{c,\mathrm{HI}}(R_j)^2}\right)\right). \quad (7)$$

$\Phi = \Phi(M_{\star,\mathrm{tot}}, q_{\mathrm{DM}}, r_s, \gamma, \rho_s)$ is computed through the MGEs, which gives us $V_{c,\Phi}^2(R) = -R(\partial \Phi / \partial R)$. $V_{c,\Phi}$ is then evaluated at $R = R_j$, where we have measurements of $V_{c,\mathrm{HI}}$ from the H I kinematics. Furthermore, we include only combinations of parameters ($M_{\star,\mathrm{tot}}$, q_{DM}, r_s, γ, ρ_s) that give rise to a $V_{c,\Phi}$ that is within 3σ of $V_{c,\mathrm{HI}}$, i.e. where $\Sigma_j[|V_{c,\Phi}(R_j) - V_{c,\mathrm{HI}}(R_j)|] < \Sigma_j[3 \times \delta V_{c,\mathrm{HI}}(R_j)]$.

The total likelihood for the 180 stars can be written as a sum of the probability and the prior, i.e. $\ln L = \Sigma_i[\ln P(V_{\mathrm{LOS,i}})] + \ln Pr_1$ for the 'Stars only' case and $\ln L = \Sigma_i[\ln P(V_{\mathrm{LOS,i}})] + \ln Pr_1 + \ln Pr_2$ for the 'Stars + Gas' case.

4 RESULTS

The marginalized model parameters for the set of MCMC runs with free q_{DM} are shown in the corner plots in Fig. 3. Black contours show
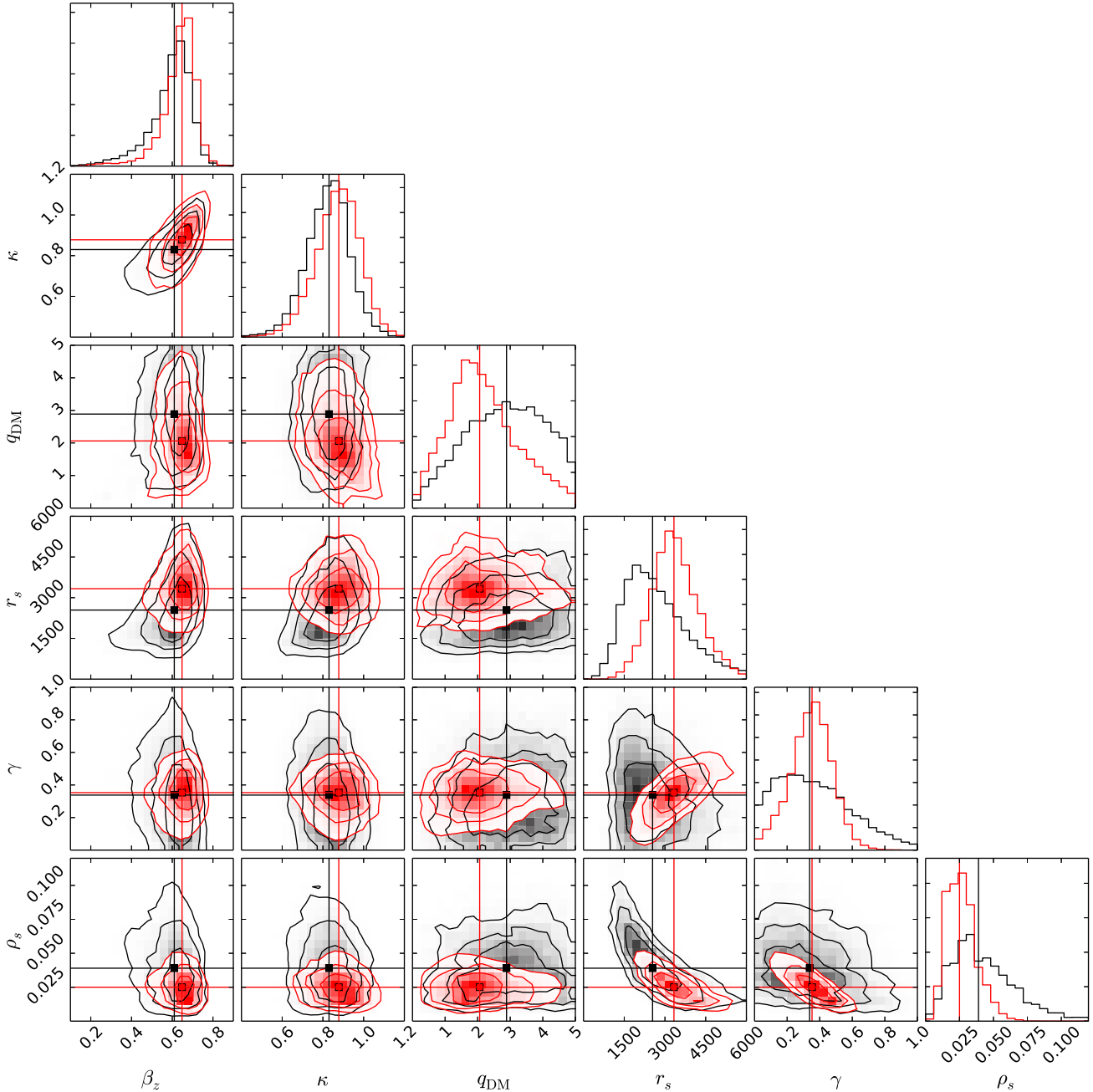
Figure 3. Marginalized parameters from the discrete Jeans models: stellar dynamical parameters β_z, κ, and DM halo parameters q_{DM}, r_s, γ, and ρ_s. Black contours show the marginalized parameter values with the models using only stellar kinematics, with contour levels 1σ, 1.5σ, and 2σ. Red contours show the models run using stellar kinematics and V_c derived from H I kinematics as a prior.

the DM halo and stellar anisotropy parameters constrained from the 'Stars only' models, and red contours show the distributions recovered from the 'Stars + Gas' models. The corresponding best-fitting parameters and their 1σ uncertainties are listed in Table 6.

4.1 DM halo properties

Both the 'Stars only' and 'Stars + Gas' models consistently prefer moderately cored DM profiles, with the posterior distributions showing $\gamma = 0.34^{+0.26}_{-0.21}$ and $0.34^{+0.12}_{-0.13}$, respectively. In Table 5, we also list the derived DM halo density slope ($-\mathrm{d}\ln \rho/\mathrm{d}\ln r$) as a function

of fixed radii (expressed as ratio to the half-light radius r_h). We show that the DM density slope crosses the cusp–core threshold of 0.5 at $\sim 0.1 r_h$ and it is better constrained in the 'Stars + Gas' model at all radii by 50–66 per cent. A prolate DM halo is preferred in both the 'Stars only' and 'Stars + Gas' model, with the 'Stars + Gas' model indicating a best-fitting $q_{DM} = 2.1^{+1.3}_{-0.9}$.

While the two models prefer parameters that agree with each other within the uncertainties, it is evident that the dark halo parameters (r_s, γ, and ρ_s) are much better constrained in the 'Stars + Gas' models when the H I kinematics are used to jointly constrain the total potential. The uncertainties in the 'Stars + Gas' models in r_s,

Table 5. Slopes of DM halo density profile ($-\mathrm{d}\ln\rho/\mathrm{d}\ln r$) as a function of radius (in ratio to the half-light radius r_h).

Radii (r_h)	0.01	0.025	0.05	0.1	0.25	0.5
Star only	$0.36^{+0.25}_{-0.20}$	$0.38^{+0.25}_{-0.20}$	$0.42^{+0.25}_{-0.20}$	$0.50^{+0.26}_{-0.21}$	$0.67^{+0.30}_{-0.23}$	$0.91^{+0.35}_{-0.26}$
Star + Gas	$0.38^{+0.14}_{-0.15}$	$0.40^{+0.13}_{-0.14}$	$0.43^{+0.12}_{-0.13}$	$0.50^{+0.11}_{-0.11}$	$0.66^{+0.09}_{-0.08}$	$0.89^{+0.12}_{-0.09}$
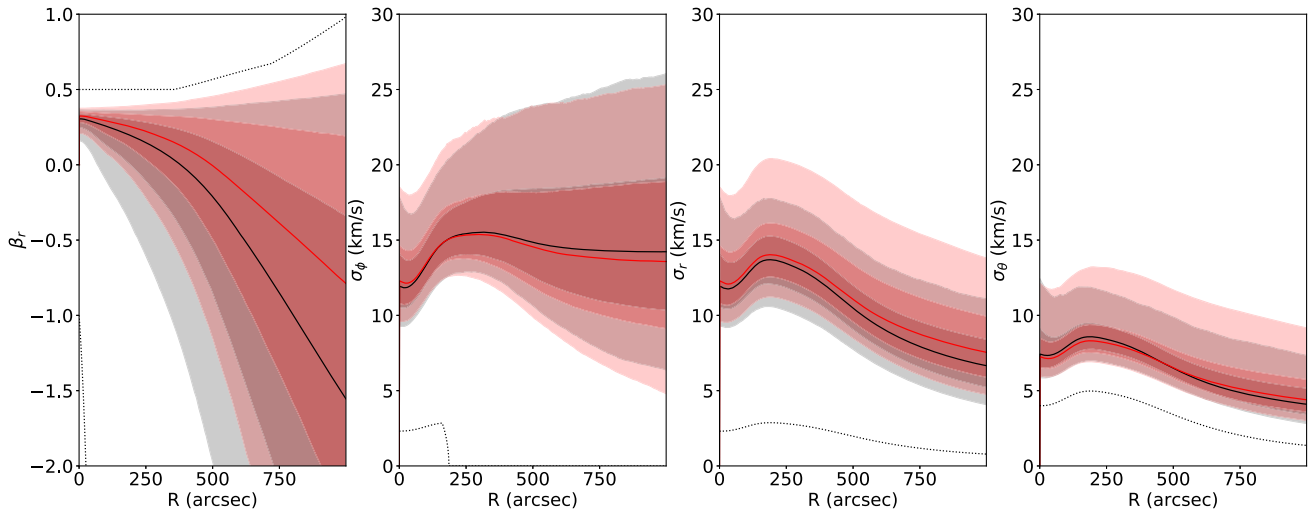
Figure 4. From left to right: the derived $\beta_r(R)$, $\sigma_\phi(R)$, $\sigma_r(R)$, and $\sigma_\theta(R)$ at $z = 0$ from our dynamical models. The thick black and red lines show the best-fitting profile and the bands show the corresponding 1σ and 2σ uncertainties for the 'Stars only' and 'Stars + Gas' models, respectively. The dotted black lines on each panel show the prior on these profiles given our priors for the free parameters as listed in Table 4.

γ, and ρ_s are smaller than the 'Stars only' model by 29 per cent, 48 per cent, and 54 per cent respectively. The halo flattening also shows a 15 per cent reduction in its uncertainty and drives towards more physical prolate values.[3]

4.2 Stellar orbital properties

Within JAM, the stellar orbital properties are described by β_z and κ. β_z describes the velocity anisotropy and is the best fit models find, $\beta_z = 0.61^{+0.07}_{-0.12}$ and $0.65^{+0.06}_{-0.09}$, respectively, for the 'Stars only' and 'Stars + Gas' models. The inclusion of gas kinematics allows a 24 per cent improvement in the constraint of β_z. It is evident that such an improvement is enabled by breaking the degeneracy between β_z and several DM halo parameters such as q_DM, r_s, and γ. κ is constrained to $0.83^{+0.09}_{-0.11}$ and $0.88^{+0.10}_{-0.11}$, respectively, for the 'Stars only' and 'Stars + Gas' models. The uncertainties of κ in both models are similar due to the fact that κ is a property that is intrinsic to the stellar kinematical map itself and is not constrained by the Jeans model.

While the anisotropy is described in JAM by β_z, we can study the more informative link with tangential velocity dispersion by computing $\beta_r = 1 - (\sigma_\phi^2 + \sigma_\theta^2)/2\sigma_r^2$. From each of the JAM models we made in the MCMC process, one can compute the individual velocity dispersions in three dimensions: σ_ϕ, σ_R, and σ_z in cylindrical coordinates, which can then be transformed into σ_ϕ, σ_θ, and σ_r in spherical coordinates. Such a calculation can be made following

equations (19)–(23), (32), and (37) from Cappellari (2008) with input MGEs describing the gravitational potential $\Phi(R, z)$ and the density profile of the kinematic tracers $\nu(R, z)$, β_z, and κ. Even though we have assumed a radially constant β_z and κ, the radially varying Φ and ν render a radially varying β_r.

Fig. 4 shows, from left to right, the derived $\beta_r(R, z = 0)$, $\sigma_\phi(R, z = 0)$, $\sigma_r(R, z = 0)$, and $\sigma_\theta(R, z = 0)$ profiles derived from 5000 randomly selected individual MCMC steps in the 'Stars only' model in thin lines, with the best-fitting profile indicated by a thick black line and the 1σ uncertainties by a black band. The corresponding profiles for the 'Stars + Gas' models are shown in red. The β_r profile transitions from a mildly radial central region to a tangentially anisotropic system in the outer regions. β_r goes from $0.32^{+0.03}_{-0.04}$ at $r = 0$ to $\beta_r = -0.35^{+0.57}_{-0.90}$ at two half-light radii ($2r_\mathrm{h} \sim 3300\,\mathrm{pc}$) for the 'Stars + Gas' models. At $r = 2r_\mathrm{h}$, the constraint on β_r improves by 27 per cent when incorporating gas kinematics in our model.

4.3 Dependence on q_DM

While both the 'Stars only' and 'Stars + Gas' models prefer a prolate halo, the flattening of the DM halo q_DM has some of the most important correlations with other parameters. While our method does not rely on the thickness of the H I layer to infer halo flattening, and thus should not be biased by assumptions the H I gas opacity (Peters et al. 2017a), given the importance of this parameter more examination is warranted. We would therefore like to understand the degeneracies between the choice of halo flattening and other parameters of interest. To assess this, we run models where the DM halo flattening is fixed to values over a grid of q_DM; ($0.25 < q_\mathrm{DM} <$
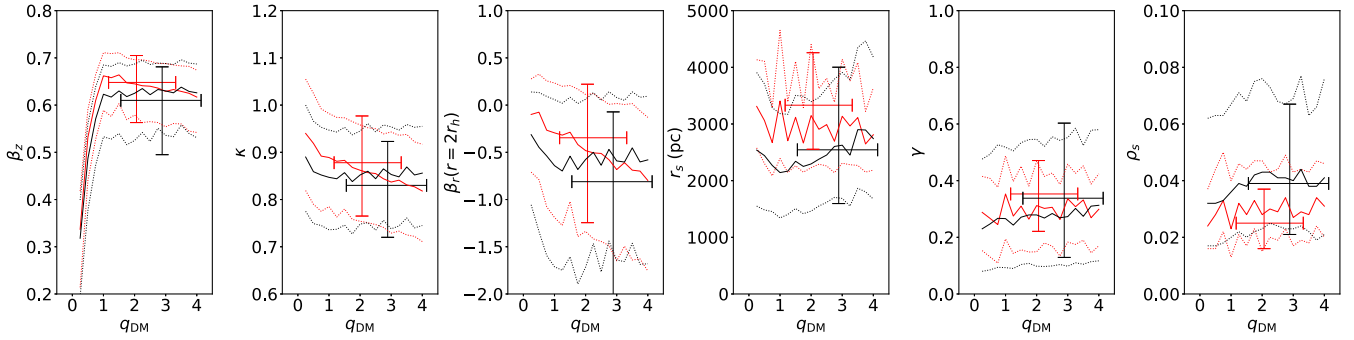
---

[3]Stability analysis for prolate, pressure-supported collisionless systems has suggested that axial ratios greater than 5:2 will result in radial orbit instabilities that quickly increase the vertical velocity distribution and reduce the eccentricity (Merritt & Hernquist 1991).

Figure 5. The best-fitting (solid line) and 1σ uncertainties (dashed lines) of the parameters constrained from the MCMC process with $q_{\rm DM}$ fixed between 0.25 and 4. Models are run at intervals of 0.25 in $q_{\rm DM}$. Black lines show the results from the 'Stars only' models and red lines show the results from the 'Stars + Gas' models. Error bars show the constrained parameters from the $q_{\rm DM}$ free runs.

Table 6. Best-fitting Jeans model parameters and 1σ uncertainties for $q_{\rm DM}$ free and $q_{\rm DM}$ models at $0.5 < q_{\rm DM} < 5.0$ at 0.5 intervals.

β_z	κ	$\beta_r\,(r=0)$	$\beta_r\,(r=r_{\rm h})$	$\beta_r\,(r=2r_{\rm h})$	$q_{\rm DM}$	r_s (pc)	γ	ρ_s (M$_\odot$ pc^{-3})
				Stars only, free $q_{\rm DM}$				
$0.61^{+0.07}_{-0.12}$	$0.83^{+0.09}_{-0.11}$	$0.30^{+0.04}_{-0.06}$	$-0.03^{+0.24}_{-0.45}$	$-0.81^{+0.74}_{-1.26}$	$2.9^{+1.3}_{-1.3}$	2544^{+1458}_{-948}	$0.34^{+0.26}_{-0.21}$	$0.039^{+0.028}_{-0.018}$
				Stars + Gas, fixed $q_{\rm DM}$				
$0.49^{+0.07}_{-0.11}$	$0.86^{+0.11}_{-0.11}$	$0.24^{+0.4}_{-0.5}$	$0.02^{+0.22}_{-0.34}$	$-0.45^{+0.58}_{-0.89}$	0.5	2442^{+1265}_{-959}	$0.25^{+0.25}_{-0.16}$	$0.032^{+0.031}_{-0.015}$
$0.62^{+0.06}_{-0.09}$	$0.85^{+0.10}_{-0.11}$	$0.31^{+0.03}_{-0.05}$	$0.03^{+0.23}_{-0.37}$	$-0.64^{+0.70}_{-1.07}$	1.0	2142^{+1041}_{-800}	$0.27^{+0.25}_{-0.17}$	$0.036^{+0.031}_{-0.016}$
$0.63^{+0.05}_{-0.09}$	$0.86^{+0.10}_{-0.11}$	$0.32^{+0.03}_{-0.04}$	$0.06^{+0.21}_{-0.36}$	$-0.54^{+0.62}_{-1.15}$	1.5	2342^{+1163}_{-834}	$0.27^{+0.26}_{-0.17}$	$0.038^{+0.030}_{-0.018}$
$0.64^{+0.05}_{-0.07}$	$0.86^{+0.10}_{-0.11}$	$0.31^{+0.03}_{-0.04}$	$0.05^{+0.21}_{-0.39}$	$-0.58^{+0.64}_{-1.14}$	2.0	3148^{+1254}_{-919}	$0.31^{+0.16}_{-0.16}$	$0.028^{+0.019}_{-0.013}$
$0.62^{+0.06}_{-0.10}$	$0.84^{+0.09}_{-0.11}$	$0.31^{+0.03}_{-0.05}$	$0.03^{+0.22}_{-0.38}$	$-0.64^{+0.69}_{-1.13}$	2.5	2453^{+1179}_{-835}	$0.28^{+0.27}_{-0.19}$	$0.041^{+0.027}_{-0.017}$
$0.63^{+0.06}_{-0.07}$	$0.84^{+0.10}_{-0.11}$	$0.32^{+0.03}_{-0.05}$	$0.05^{+0.22}_{-0.36}$	$-0.59^{+0.67}_{-1.05}$	3.0	3136^{+1006}_{-826}	$0.34^{+0.12}_{-0.15}$	$0.027^{+0.016}_{-0.010}$
$0.64^{+0.06}_{-0.08}$	$0.87^{+0.09}_{-0.11}$	$0.32^{+0.03}_{-0.04}$	$0.09^{+0.27}_{-0.33}$	$-0.45^{+0.49}_{-1.01}$	3.5	2900^{+1451}_{-1034}	$0.27^{+0.25}_{-0.17}$	$0.038^{+0.025}_{-0.016}$
$0.63^{0.06}_{-0.09}$	$0.86^{+0.10}_{-0.11}$	$0.31^{+0.03}_{-0.05}$	$0.05^{+0.22}_{-0.37}$	$-0.58^{+0.67}_{-1.10}$	4.0	2741^{+1438}_{-1067}	$0.31^{+0.27}_{-0.20}$	$0.041^{+0.035}_{-0.020}$
				Stars + Gas, free $q_{\rm DM}$				
$0.65^{+0.06}_{-0.09}$	$0.88^{+0.10}_{-0.11}$	$0.32^{+0.03}_{-0.04}$	$0.13^{+0.18}_{-0.30}$	$-0.35^{+0.57}_{-0.90}$	$2.1^{+1.3}_{-0.9}$	3331^{+926}_{-778}	$0.34^{+0.12}_{-0.13}$	$0.025^{+0.012}_{-0.009}$
				Stars only, fixed $q_{\rm DM}$				
$0.53^{+0.06}_{-0.08}$	$0.92^{+0.11}_{-0.13}$	$0.26^{+0.03}_{-0.04}$	$0.15^{+0.15}_{-0.28}$	$-0.08^{+0.25}_{-0.72}$	0.5	3061^{+1046}_{-759}	$0.27^{+0.14}_{-0.14}$	$0.028^{+0.016}_{-0.012}$
$0.66^{+0.05}_{-0.18}$	$0.89^{+0.09}_{-0.10}$	$0.33^{+0.02}_{-0.04}$	$0.14^{+0.18}_{-0.31}$	$-0.29^{+0.53}_{-0.90}$	1.0	3406^{+1247}_{-1014}	$0.35^{+0.13}_{-0.16}$	$0.023^{+0.017}_{-0.010}$
$0.66^{+0.05}_{-0.06}$	$0.88^{+0.09}_{-0.10}$	$0.33^{+0.02}_{-0.03}$	$0.15^{+0.16}_{-0.15}$	$-0.29^{+0.50}_{-0.74}$	1.5	3118^{+984}_{-855}	$0.31^{+0.14}_{-0.15}$	$0.028^{+0.016}_{-0.011}$
$0.64^{+0.05}_{-0.07}$	$0.86^{+0.10}_{-0.11}$	$0.32^{+0.03}_{-0.03}$	$0.09^{+0.19}_{-0.28}$	$-0.48^{+0.53}_{-0.86}$	2.0	3148^{+1254}_{-919}	$0.31^{+0.16}_{-0.16}$	$0.028^{+0.019}_{-0.013}$
$0.64^{+0.05}_{-0.07}$	$0.86^{+0.09}_{-0.11}$	$0.32^{+0.03}_{-0.04}$	$0.08^{+0.18}_{-0.31}$	$-0.51^{+0.58}_{-0.93}$	2.5	2989^{+818}_{-730}	$0.31^{+0.12}_{-0.14}$	$0.029^{+0.015}_{-0.010}$
$0.63^{+0.06}_{-0.07}$	$0.84^{+0.11}_{-0.11}$	$0.31^{+0.03}_{-0.04}$	$0.03^{+0.22}_{-0.32}$	$-0.68^{+0.70}_{-0.97}$	3.0	3136^{1006}_{-829}	$0.34^{+0.12}_{-0.15}$	$0.027^{+0.016}_{-0.010}$
$0.63^{+0.05}_{-0.07}$	$0.83^{+0.11}_{-0.11}$	$0.31^{+0.03}_{-0.03}$	$0.03^{+0.22}_{-0.32}$	$-0.69^{+0.70}_{-0.95}$	3.5	3113^{+969}_{-844}	$0.33^{+0.12}_{-0.14}$	$0.028^{+0.015}_{-0.010}$
$0.64^{+0.05}_{-0.07}$	$0.86^{+0.10}_{-0.11}$	$0.31^{+0.03}_{-0.04}$	$0.00^{+0.21}_{-0.31}$	$-0.80^{+0.65}_{-0.96}$	4.0	3148^{+1254}_{-919}	$0.32^{+0.16}_{-0.16}$	$0.028^{+0.019}_{-0.013}$

4.0, at intervals of 0.25), in order to evaluate the effect of $q_{\rm DM}$ on the stellar dynamical and DM properties.

The best-fitting parameters for these constrained models are plotted as a function of $q_{\rm DM}$ in Fig. 5 in solid lines, with the respective 1σ uncertainties indicated by dashed lines. The free parameters are then reported in intervals of $q_{\rm DM} = 0.5$ in Table 6. Black lines show the parameter constraints from the 'Stars only' models and the red lines show the parameter constraints from the 'Stars + Gas' models. The best-fitting parameters from the models where $q_{\rm DM}$ is free to vary are also shown by the error bars for reference.

In both the 'Stars only' and 'Stars + Gas' cases, β_z shows a well-known degeneracy with $q_{\rm DM}$ at $q_{\rm DM} \lesssim 1$; a flatter DM halo gives a

lower β_z. Similar degeneracies also exist between $q_{\rm DM}$ and β_r. The derived β_r values at $r = 0$, $r_{\rm h}$, and $2\,r_{\rm h}$ are listed in Table 6. The degeneracies are stronger at large radii ($r \gtrsim r_{\rm h}$), with a higher $q_{\rm DM}$ corresponding to a lower β_r (more tangential anisotropies). Also, the degeneracies between $q_{\rm DM}$ and β_r extend to much higher $q_{\rm DM}$, all the way up to $q_{\rm DM} = 4$. Curiously, such $\beta_r - q_{\rm DM}$ degeneracy is only present in the 'Stars + Gas' models but not in the 'Stars only' models. The other stellar orbital parameter κ also shows a degeneracy in the sense of higher $q_{\rm DM}$ leading to lower κ, again such a degeneracy is only present in the 'Stars + Gas' models.

Reassuringly, the inner slope of the DM density profile, γ, appears robust to the choice of halo shape. As in the case of the freely varying $q_{\rm DM}$ models, the DM parameters, r_s, γ, and ρ_s, are better constrained
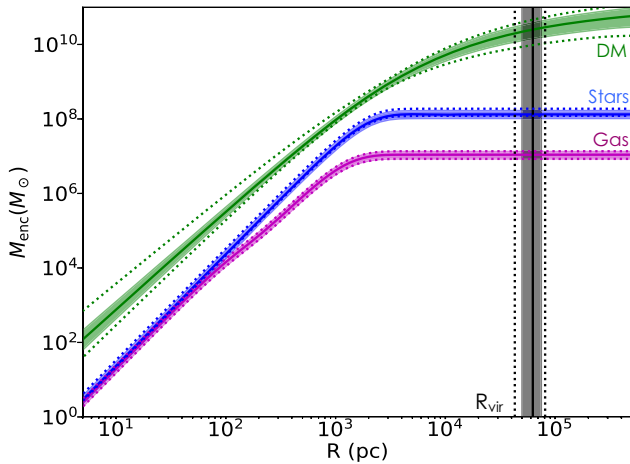
Figure 6. Enclosed mass profiles. The stellar, gas, and DM profile from the best-fitting 'Stars + Gas' model are plotted in magenta, blue, and green respectively. Vertical lines indicate the virial radius. The width of the bands gives the 1σ uncertainties. Dotted lines show the corresponding constraints from the 'Stars only' dynamical models.

on average by 27 per cent, 39 per cent and 46 per cent at all q_{DM} when we include $V_{c, HI}$ as a constraint.

5 DISCUSSION

Using discrete Jeans models, together with circular velocity constraints from the H I gas rotation curve, we have derived tight constraints on the DM halo shape and density profile. Additionally, we derive, for the first time, the stellar velocity anisotropy profile of a dIrr. Below we discuss the implications of our results for modified gravity and DM theories, and formation models of dwarf galaxies.

5.1 WLM's DM halo properties in the context of ΛCDM cosmology

The halo parameters from our best-fitting models can be used to reconstruct the three-dimensional mass distribution in WLM with high confidence. Here we examine the inner density profile and flattening of the DM halo with respect to simulations of galaxy formation in a ΛCDM framework.

5.1.1 DM density profile

Fig. 6 shows the DM and stellar enclosed mass profiles (within a sphere) derived from our 'Stars + Gas' and q_{DM} free dynamical model in green and purple, respectively. The DM virial mass, M_{vir},[4] is constrained to within $2.50^{+1.75}_{-1.23} \times 10^{10}\,M_\odot$ in the 'Stars + Gas' model and $2.00^{+2.89}_{-1.24} \times 10^{10}\,M_\odot$ in the 'Stars only' model – in good agreement with Leaman et al. (2012), who used an SIS and NFW fit to the asymmetric-drift-corrected stellar kinematics.

The derived stellar-to-halo mass ratio is therefore $\log_{10}(M_\star/M_{vir}) = -3.4 \pm 0.3$, which is slightly higher than the stellar-mass–halo-mass relation found by Moster et al. (2010) $\log_{10}(M_\star/M_{vir}) = -3.1 \pm 0.1$ using the same $M_\star$ value, but consistent within

---

[4]M_{vir} here is defined as the enclosed mass within the virial radius R_{vir}, where the mass density $\rho(R = R_{vir}) = 200\rho_{crit}$ and the critical density ρ_{crit} is calculated with a Hubble constant $H = 67.1$.

the uncertainties. When we run models with a prior on the stellar mass of $M_\star = 4.3 \times 10^7\,M_\odot$ (± 50 per cent), a larger value favoured from star formation history studies of WLM (Leaman et al. 2017), we derive a higher $\log_{10}(M_\star/M_{vir}) = -2.8 \pm 0.2$. In Fig. 7, we show the $\log_{10}(M_\star/M_{vir})$ from the 'Stars only' and 'Stars + Gas' models with a prior $M_\star = 1.1 \times 10^7\,M_\star$ (± 50 per cent) in black and red, and for completeness a 'Stars + Gas' model with prior $M_\star = 4.3 \times 10^7\,M_\odot$ (± 50 per cent) in orange.

The DM halo concentration ($c \equiv r_{vir}/r_{-2}$, where r_{vir} is the virial radius and r_{-2} is the radius at which the logarithmic slope of the DM density is $d\ln\rho_{DM}/d\ln r = -2$) for our best-fitting models is close to the expected mass–concentration (M_{vir}–c) relation from DM-only simulations (Dutton & Macciò 2014). Given our derived M_{vir}, the M_{vir}–c relation found by Dutton & Macciò (2014) would suggest $c = 12.1^{+0.9}_{-0.6}$, consistent within the uncertainties to our inferred halo concentration of $c = 11.4 \pm 1.6$.

Our analysis suggests that WLM has a relatively cored DM density distribution with a best fit to the inner slope of the density profile $\gamma = 0.34 \pm 0.12$. This value is robust to the recovered DM halo shape (q_{DM}), and has an expected correlation with the scale length and normalization of the DM halo, r_s and ρ_s. The central density profile of low-mass dwarfs is an important tracer of internal and external evolutionary processes in dwarf galaxies (e.g. Zolotov et al. 2012; Brooks & Zolotov 2014; Oñorbe et al. 2015). Using hydrodynamical simulations, Di Cintio et al. (2014) found that the feedback process that alters the inner slope of DM haloes also modifies the final stellar-to-halo-mass ratio ($M_\star/M_{vir}$), and a relation between the two was parametrized as

$$\gamma = -0.06 + \log_{10}[(10^{X+2.56})^{-0.68} + (10^{X+2.56})], \quad (8)$$

where $X = \log_{10}(M_\star/M_{vir})$.

In the mass range of WLM, a higher $M_\star/M_{vir}$ would translate to a flatter inner slope (smaller γ) – as the stellar feedback is proportionally more effective at causing halo expansion due to rapid gas expulsion in the relatively shallow potential well. For our derived $M_\star/M_{vir}$, the Di Cintio et al. (2014) predicts $\gamma = 0.5 \pm 0.2$, consistent within the errors with the γ derived from our models of $\gamma = 0.34 \pm 0.12$. If we use the 'Stars + Gas' model ran with $M_\star = 4.3 \times 10^7$, the derived value from Di Cintio et al. (2014): $\gamma = 0.25 \pm 0.16$ is in excellent agreement with our modelled value: $\gamma = 0.23 \pm 0.12$ (as shown in orange contours in the bottom panel of Fig. 7). To compare to the simulations from Read et al. (2016), we have also fitted our derived DM density profile with a cored-NFW profile and found a core size of $r_{core} = 1257^{+318}_{-269}$ pc. In those simulations, the typical core size was found to scale with the stellar half-mass radius as $r_c \sim 1.75\,r_h$. Our derived core size is slightly smaller than this finding, with the ratio $0.6 \leq r_c/r_h \leq 1.0$ for our best-fitting models. However, we note that taking the exponential scale length of the disc ($r_d = 987$ pc; Leaman et al. 2012) gives $0.98 \leq r_c/r_d \leq 1.65$.

In the context of ΛCDM galaxy formation, WLM appears to have been able to efficiently convert its presumably primordial NFW DM cusp into a shallower density profile over a Hubble time of star formation and feedback. This process has occurred, and yet left the system with: an exponential and smoothly distributed intermediate-age population (Leaman et al. 2012), no quenched SFH (Weisz et al. 2014), a metallicity distribution function and age–metallicity relation in agreement with a simple leaky box model (Leaman et al. 2013), and a stellar age–velocity dispersion relation consistent with gradual dynamical cooling of the gas (Leaman et al. 2017). These all suggest that the core-creation process need not always quench the system, nor be catastrophic to the structural, dynamical, or chemical properties
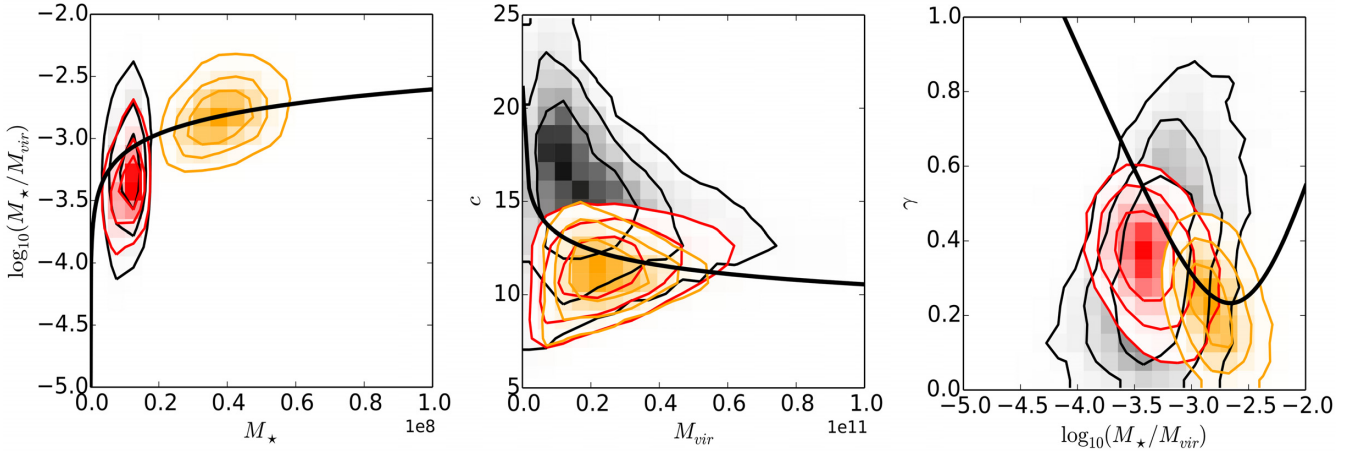
Figure 7. Contours showing the constrained values as labelled from models with prior $M_\star = 1.1 \times 10^7 \, M_\star$ (± 50 per cent) 'Stars only (black) and 'Stars + Gas' (red), and with prior $M_\star = 4.3 \times 10^7 \, M_\star$ (± 50 per cent) 'Stars + Gas' in orange. The $M_\star$–$M_\star/M_{vir}$ relation from Moster et al. (2010), the mass–concentration relation from Dutton & Macciò (2014), and the $M_\star/M_{vit}$–γ relation from Di Cintio et al. (2014) are shown as thick black lines from the left- to right-hand panels.

of the galaxy – at least in this virial mass range. A more detailed joint analysis of the chemical and kinematic properties may help disentangle whether the core creation process was bursty as expected from feedback scenarios (e.g. El-Badry et al. 2017) or more gradual as in the case of self-interacting DM.

Previous numerical studies have also explained many of WLM's properties in terms of a feedback-based alteration to the underlying NFW profile. For example, using a set of hydrodynamical simulations for dwarf galaxies, Teyssier et al. (2013) were able to reproduce the spatial and dynamical structural properties of WLM, while at the same time transforming the DM halo from cusped to core by stellar feedback from bursty star formation. Two WLM-like galaxies with exponential stellar discs of $V/\sigma \sim 1$ were also formed in the study by Shen et al. (2014) from a fully cosmological high-resolution ΛCDM simulation, again with baryonic feedback playing an important role. The dwarf galaxies from their simulation lie on the observed mass–metallicity relation observed in the Local Group dwarfs, suggesting that the feedback process can operate in a non-destructive fashion for isolated dwarfs.

This provides a counter example to systems such as ultra-diffuse galaxies (UDGs), which may acquire their extended structure and old stellar populations partly due to the same feedback processes (Di Cintio et al. 2017), but with more extreme consequences on the system. Given that some UDGs are estimated to be of comparable virial mass to WLM (Beasley & Trujillo 2016), understanding what different conditions during the galaxy's lifetime (e.g. star formation density and environment) lead to such disparate final states is an avenue worth further study. For example, the resultant decrease in central density and gas concentration may be extremely important for evolutionary changes of dwarf satellites, as demonstrated by Brooks & Zolotov (2014). Finding present-day observational signatures that can trace the rapidity and strength of the potential fluctuations may provide further insight into the time-scales, and mechanisms with which the DM core is growing, and can potentially differentiate feedback-driven or particle scattering processes (e.g. gas and stellar spatial distributions; Mondal, Subramaniam & George 2018). This will be discussed in the subsequent section; however, to first order the DM halo density profile we derive is in excellent agreement with the predictions from simulations that incorporate the effect of feedback-driven halo expansion in a CDM framework.

5.1.2 DM halo flattening

We now turn to the shape (axial ratio) of the DM halo inferred from our dynamical models. Table 6 shows that in both the 'Stars + Gas' and 'Stars only' models, a prolate DM halo is preferred, with $q_{DM} \sim 2 \pm 1$ inferred from the 'Stars + Gas' model. Pure DM ΛCDM cosmological simulations show that DM haloes with our derived M_{vir} for WLM have an average short-to-long axial ratio of ~ 0.7 at the virial radii r_{vir} (Macciò, Dutton & van den Bosch 2008). Butsky et al. (2016) find similar q_{DM} at r_{vir} with high-resolution DM-only simulations. They, however, extend the analysis towards the inner region and show that over the radii where our stellar kinematics cover (< 5 per cent r_{vir}), DM haloes of $M_{vir} \sim 10^{10} \, M_\odot$ have an even lower average short-to-long axial ratio of ~ 0.5 and are predominantly prolate.

Those authors used a suite of high-resolution hydrodynamical simulations and showed that while baryonic feedback does not have noticeable effects on q_{DM} at the virial radii, it may change q_{DM} in the inner region of the halo depending on the M_{vir} of the galaxy. The inner region ($< 0.12 \, r_{vir}$) of DM haloes evidently becomes more spherical for galaxies with $M_{vir} > 10^{11} \, M_\odot$. For galaxies with M_{vir} similar to the one we derived for WLM however, q_{DM} does not significantly differ from DM-only simulations, meaning that a prolate halo with a short-to-long axial ratio of ~ 0.5 is still expected, corresponding to a q_{DM} of ~ 2. This is in excellent agreement with the q_{DM} derived from our 'Stars + Gas' model. Although a spherical/oblate halo has been ruled out at the 1σ level, such geometries are still possible within the 2σ level. Given the evident $q_{DM} - \beta$ (especially β_r) degeneracies, future proper motion measurements will help us to further constrain the halo geometry. Similar values consistent with our finding for WLM are seen in the study of González-Samaniego et al. (2017) with the FIRE simulations of dwarf galaxies.

As we shall see below, the halo shape measurement is a strong prediction of our models, and together with the DM density slope, may offer one of the most powerful lever arms to differentiate baryonic feedback plus CDM scenarios from self-interacting DM models.

5.2 WLM as a test of self-interacting DM models and modified gravity

The simultaneous recovery of a density core and a prolate DM halo is extremely important in understanding the viability of models of
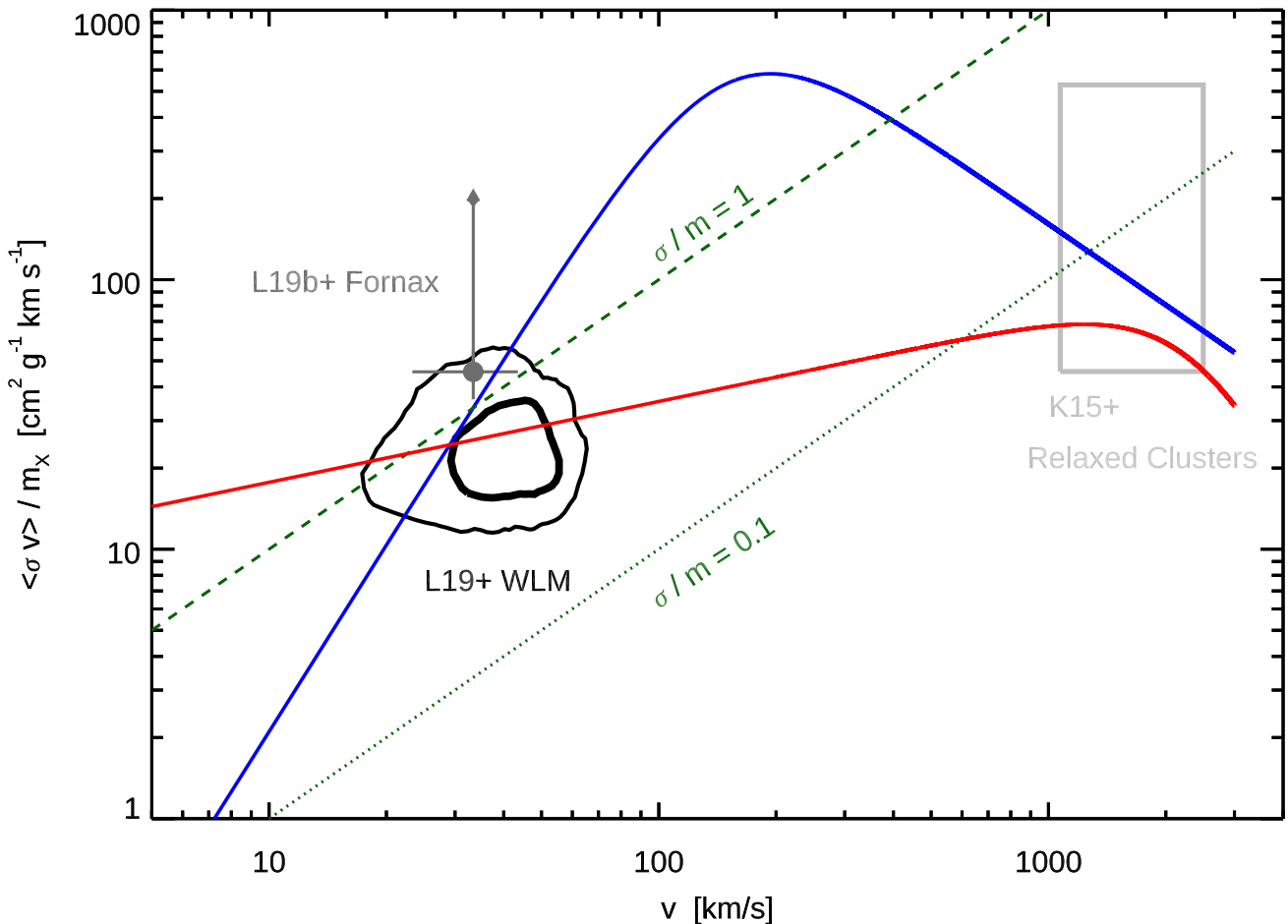
Figure 8. Velocity-averaged interaction cross-sections as a function of characteristic halo velocities. The self-interacting DM particle cross-section necessary to reproduce the density profile of WLM is shown with black contours at the 1σ and 2σ levels. Limits for the Fornax dSph from Leung et al. (2020) are shown in grey. Dotted and dashed lines show the cross-sections for *velocity-independent* SIDM models of $\sigma/m_X = 0.1$ and 1 cm^2 g^{-1} respectively. Two examples of *velocity-dependent* SIDM models that are compatible with the dwarf galaxy limits, as well as constraints from galaxy clusters [as marked by the grey box (Kaplinghat et al. 2016)] are shown in red and blue lines, with parameters indicated. However, whether they also preserve aspherical geometries in dwarfs is not yet quantified in simulations.

non-standard DM, e.g. thermal relic, self-interacting (SIDM), Bose–Einstein condensate (BECDM or 'fuzzy') DM. We have previously seen the good agreement between our observations and predicted values for the DM inner density profile slope and axial ratios in CDM simulations with baryonic feedback. These models work under the assumption that the DM itself is collisionless and the modifications to the density profile arise indirectly due to stellar feedback rapidly changing the potential well through gas expulsion (cf. Pontzen & Governato 2012).

Galaxy formation simulations where the DM particle may have a self-interaction cross-section can also produce modifications to the central density profile. In this case, the particle self-interactions, which have a higher rate of occurrence in the denser central regions, result in elastic (or inelastic; Vogelsberger et al. 2019) scattering of particles (of order one event per particle per Hubble time) and the formation of a density core in the galaxy DM distribution (Vogelsberger, Zavala & Loeb 2012; Peter et al. 2013).

To place our results in the context of such SIDM theories, we compute the model DM density at the core radius $\rho(r_c)$ using the best-fitting 'Stars + Gas' profile parameters, and derive the likely velocity-weighted interaction cross-section for SIDM models to produce this

cored profile:

$$\frac{\langle \sigma v \rangle}{m_X} = \{\rho(r_c)t_{halo}\}^{-1}, \qquad (9)$$

where m_X is the mass of the SIDM particle candidate and t_{halo} is the collapse time of the DM halo, here taken to be 13 Gyr. Fig. 8 plots the constraints on the cross-section using our derived halo properties for WLM. Also shown are the limits on the same quantity for the Fornax dSph, from Leung et al. (2020) based on modelling of that dwarf galaxy's GC dynamics. Velocity independent scattering predictions for different SIDM cross-sections are shown as green straight lines. Constraints from high-mass galaxy clusters indicate that such velocity-independent SIDM models require $\sigma/m_X \lesssim 0.1$ cm^2 g^{-1} (e.g. Kaplinghat, Tulin & Yu 2016; grey box in Fig. 8), which is the dotted green line shown in our figure. Those studies and others suggest that local dwarf galaxies are more consistent with $\sigma/m_X \sim 0.1$–10 cm^2 g^{-1}. From the 'Stars + Gas' model, we derive a σ/m_X of $0.57^{+0.42}_{-0.20}$ cm^2 g^{-1} for WLM.

The mismatch between the required velocity-independent cross-sections needed for local dwarfs and high-mass galaxy clusters has led to *velocity-dependent* scattering models to be preferred. We show

three examples as the red, green, and blue lines in Fig. 8, all of which pass through the combined constraints of WLM and Fornax, however only one of these with the high peak velocity dependence ($v_{max} = 400$ km s^{-1}) is also consistent with the cluster measurements of Kaplinghat et al. (2016). The constraints posed by WLM do not a priori prefer a velocity dependence to the self-interacting DM models – however, as we shall see, the *simultaneous finding of a core and a prolate halo may rule out the velocity-independent models*, as these are reported to become thermalized and spherically symmetric in their inner regions for the values needed here (Peter et al. 2013).

The final core sizes generated from DM scattering can be ∼1 kpc, just as in baryonic feedback + CDM scenarios. Therefore, additional signatures may be needed to differentiate whether a detected DM core is a unique consequence of baryonic feedback or self-interaction modifications to the DM density profile. The time-scale for the core to form may be longer in SIDM; however, this depends on the particular baryonic subgrid prescriptions adopted (e.g. star formation or feedback injection efficiencies). For example, Fry et al. (2015) showed that the growth rate and final size of the DM core in haloes with $V_{max} \leq 30$ km s^{-1} may be largely the same in self-interacting DM with or without baryonic feedback – though this again depends on the mass range and adopted cross-section. While there could be chemical and/or phase space signatures that may help understand the precise mechanism(s) better, the sparsity of detailed abundances and numbers of observed stars in low-mass galaxies makes this a daunting process. What then may be a potential way to understand whether self-interacting DM or feedback scenarios have generated observed cores in dwarf galaxies?

The scattering process that generates a core in self-interaction models may potentially sphericalize the mass distribution, as the interactions are isotropic. This means that the core formation process in pure self-interaction DM models could result in spherical mass distributions in the inner regions of the haloes. The simultaneous quantification of DM density profile slope and axial ratio has unfortunately only been reported as far as we can tell, in simulations of high-mass ($M_{vir} \geq 10^{11}$) haloes (Peter et al. 2013). In these simulations, haloes with $\sigma/m_X = 1$ cm^2 g^{-1} that form increasingly cored density distributions (approaching $\gamma \sim 0.4$) become approximately spherical ($c/a \sim 0.9$). For lower cross-sections of $\sigma/m_X = 0.1$ cm^2 g^{-1}, density profile slopes of $\gamma = 0.8$ still retain axial ratios of $c/a \sim 0.6$, but these values are not nearly as cored as what we find, and are only reported for haloes of $M_{vir} \sim 10^{13-14}$ M$_\odot$. Most importantly, these low values for the cross-section are already ruled out on the basis of the WLM DM density profile.

Simulations that explore the halo shape of velocity-independent SIDM models in the presence of baryons have found that the core creation process can occur with non-spherical final halo shapes in the inner regions (Sameie et al. 2018). However, in that case the inner halo progressed towards the axial ratios of the embedded baryonic distribution, which in the case of WLM would be *oblate* with $c/a = 0.4$–0.6 (Leaman et al. 2012). Fitts et al. (2018) simulated dwarf galaxies in our halo mass range with SIDM and baryonic components and found similar behaviour, whereby baryons were the dominant process in altering the DM halo profiles (either indirectly through feedback or afterwards through contraction) – however, there was no reported characterization of the halo shapes. Velocity-dependent SIDM models presented in Vogelsberger et al. (2012) show indications that high-mass haloes can preserve their shapes in the presence of central density modifications; however, these simulations were again with MW-mass haloes.

There is clear need for numerical simulations to quantify the simultaneous evolution of the DM density inner slope and halo shape

in the presence of baryons for haloes of mass $M_{vir} \sim 10^{10}$ M$_\odot$. Robles et al. (2017) looked at one dwarf in the FIRE simulations that has a stellar mass slightly lower than WLM ($M_\star \sim 10^7$). The simulations of SIDM with $\sigma/m = 1$ cm^2 g^{-1} with feedback and CDM with feedback show the same qualitative behaviour as the Peter et al. (2013) study – SIDM sphericalizes the haloes as it generates a core in the low-mass galaxies also. *WLM's recovered prolate DM halo with $q_{DM} = 2$, density slope of $\gamma = 0.34$, and core of size $r_c = 1257$ pc may provide a strong constraint that velocity-dependent self-interacting DM models need to satisfy.*

Axion-mixed DM models or BECDM models also predict a relation between the core size and halo mass – however, in this case the core is inherent to the structure formation in these models. Following Schive et al. (2014), in the case of ultralight BECDM, the soliton core size is related to the halo virial mass and effective particle mass (m_ψ) as

$$r_c = 1.5\text{kpc} \left(\frac{M_{vir}}{10^9 M_\odot} \right)^{-1/3} m_\psi^{-1}. \tag{10}$$

For WLM's constraints on the core size and virial mass, we find $0.24 \times 10^{-22} \leq m_\psi \leq 1.66 \times 10^{-22}$ eV/c^2, consistent with constraints from large-scale structure studies. Similar to the above SIDM studies, more work is needed to quantify the halo axial ratios in low-mass haloes (with non-negligible baryon fractions), in these or other alternative cosmological models (e.g. ETHOS; Vogelsberger et al. 2016).

Finally, we comment briefly on the implications of our inferred dark mass distribution on theories of modified gravity such as MOND (Milgrom 1983). WLM is an interesting test case in that it has well-defined inclination and measurements of a circular velocity curve from H I kinematics (Iorio et al. 2017), stellar velocity dispersion, and anisotropy (Leaman et al. 2012 and this work) and an intrinsic thickness (Leaman et al. 2012). Our discrete Jeans model for WLM suggests that there is an extended dark mass distribution around WLM, with a prolate axial ratio of 2:1. MOND will reproduce the contributions to the observed circular velocity field by altering the acceleration field in the outer regions – however, this can only mimic a mass distribution with $q = 0.9$. WLM is in the deep MOND regime and its extreme isolation means that an external field effect cannot be invoked to alleviate discrepancies with MOND predictions in the outer disc. The prolate dark mass distribution inferred for WLM may represent a significant obstacle for describing the dynamics and structure of this dwarf galaxy with MOND (see also Helmi 2004). A follow-up paper will present a more detailed discussion and analysis of WLM's stellar structure, dynamics, and enclosed mass profile with respect to MOND.

5.3 Tangential velocity anisotropy in an evolutionary context for dwarf galaxies

Determining velocity anisotropy in systems with a single type of kinematic tracer has long been assumed to be difficult due to the mass-anisotropy degeneracy inherent to spherical Jeans equations. For a couple of well-studied dSphs, authors have used discrete Jeans models or orbit-based Schwarzschild superposition models to better constrain the velocity anisotropy, and found that the anisotropy becomes increasingly more tangential with radius, for both Sculptor (Zhu et al. 2016) and Fornax (Kowalczyk et al. 2018). In subsequent work using proper motions measured from *Gaia*, Massari et al. (2018) determined a median radial anisotropy of $\beta_r \sim 0.46$ for Sculptor, but only for the inner region $r \lesssim 0.35\, r_h$.

Interestingly, WLM also demonstrates a mild radial anisotropy in the inner region of $r \lesssim 1\,r_{\rm h}$, which turns to be tangentially biased towards larger radii ($\beta_r \sim -0.5$). To demonstrate the similarities between the β_r profile we obtained from the dIrr WLM and the dSphs, we overlay the β_r profiles obtained by Zhu et al. (2016) for Sculptor (blue) and Kowalczyk et al. (2018) for Fornax (green) on top of the one we obtained from the 'Stars + gas' $q_{\rm DM}$ free model (red) in Fig. 9. There are clear similarities in all three dwarfs, with the best-fitting anisotropy profile becoming increasingly tangential in the outer regions [albeit the derived uncertainties for both Fornax by Kowalczyk et al. (2018) and WLM by us allow for slightly radial anisotropy of up to $\beta_r \sim 0.2$].

The interpretation of any anisotropy profile is not straightforward, nor unique. For example, dissipationless gravitational collapse can lead to an isotropic core, surrounded by an envelope of radially anisotropic orbits (van Albada 1982) – however, the same config-uration is seen to occur in simulations of dwarfs that undergo bar-buckling (Mayer 2010). There, bar formation can be triggered by strongly radial anisotropy, before undergoing a bending instability that erases the radial anisotropy (preferentially increasing the vertical velocity dispersion). In higher mass haloes, the reconfiguration of stellar orbits due to minor merging can reproduce the typically radial anisotropic profiles seen for MW-mass galaxies, with transient tangential anisotropy appearing due to recent major accretion or fly-bys of satellites (Loebman et al. 2018).

Alternatively, simulations have shown that tangential anisotropy can be caused by preferential stripping of stars on prograde and radial orbits in a tidal field (e.g. Henon 1970; Keenan & Innanen 1975; Baumgardt & Makino 2003; Read et al. 2006; Hurley & Shara 2012). The tangential anisotropy in some dSphs, found especially at large radii ($r \gtrsim r_{\rm eff}$, the effective radius), has often been used to support the scenario in which dIrrs are transformed into dSphs via tidal processing.

The negatively biased β_r derived at large radii from our dynamical models for WLM puts the last scenario into question. The velocity anisotropy profiles we find in the dIrr WLM, being nearly isotropic in the centre and increasingly tangential towards the outskirts of the galaxy (reaching $\beta_r = -0.35^{+0.57}_{-0.90}$ at $r = 2\,r_{\rm h}$), are very similar to those found in the aforementioned dSphs.[5] WLM is an extremely isolated galaxy ($D_{\rm MW, M31} \sim 1$ Mpc; see fig. 1 of Leaman et al. 2012), with Local Group barycentric velocity suggesting that it has last been in the proximity of a massive neighbour ~ 11 Gyr ago.

WLM's derived β_r profile thus provides an environmentally unprocessed baseline for using stellar kinematics to understand the evolutionary similarities or links between dIrrs and dSphs. First of all, the similarity of β_r between these dSphs and an isolated dIrr implies that the negative β_r seen in dSphs need not be a result of tidal stripping. The orbital information of both Sculptor and Fornax inferred from proper motion measurements done with *Gaia* also has weakened the case that they have been tidally stripped (Fritz et al. 2018), as the derived pericentres of these two galaxies are both 50 kpc and N-body simulations on the effects of tides based on
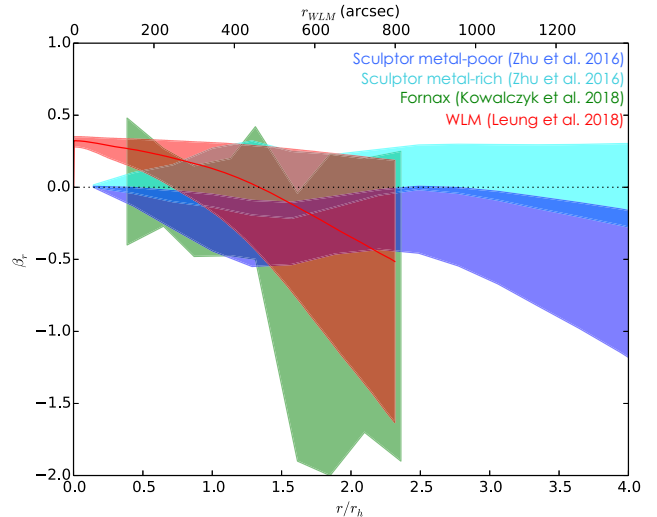

Figure 9. Derived WLM β_r profile (in red) overlaid on the β_r profiles of two dSphs, Sculptor in blue (Zhu et al. 2016) and Fornax in green (Kowalczyk et al. 2018), as an illustration of the similarities in their overall trend. The metal-poor population of Sculptor plotted in cyan has more radial anisotropy but is only dominant in the inner $\sim 1.5\,r_{\rm h}$.

observationally motivated orbits on both Sculptor (Iorio et al. 2019) and Fornax (Battaglia, Sollima & Nipoti 2015).

Given the other evidence in its dynamical and chemical evolu-tion for a quiescent existence, it would seem that the tangential anisotropy in this case is either primordial or imparted through some other mechanism. Whatever the mechanism to form or impart this anisotropy profile, the similarity between the dIrr and dSphs may also suggest that the transformation from dIrr to dSph is not a violent or dynamical one. Indeed, the stellar kinematics, chemistry, and SFHs of some of the *massive* dSphs are becoming increasingly similar to the dIrrs where studies of both are done to comparable depths (e.g. Wheeler et al. 2017). In that case, the present-day differences may only become extreme where there is significantly early infall, for example for more low-mass nearby dSphs – and in other cases perhaps the difference is only quenching of the SF due to gentle ram pressure in the outer halo of the MW's CGM.

If extreme tidal processing is not playing a role in determining the anisotropy profile, we might ask if it is something intrinsic to the formation of galaxies of this mass regime? Some studies have looked at the relative role of gas pressure support in the initial gas disc of dwarfs (Kaufmann, Wheeler & Bullock 2007) or spatial distribution of star formation and stellar populations in dwarf galaxies (Schroyen et al. 2011). However, neither study provided quantification of the newly formed stellar anisotropy profiles. The details of how any aspects of the gas inflow history (e.g. Kereš et al. 2005) or turbulence map into 3D stellar kinematics need additional study, but may provide help in understanding the similarities in Fig. 9.

If the anisotropy at formation is not preserved until present day, the similar profiles for two of the bright classical dSphs and WLM indicate that any evolutionary process that generates tangential anisotropy may need to operate in a generic galaxy of this mass. Such processes could either be connected to dynamical scattering of stars or the dynamical mixing of gas at the epoch of formation of the surviving stellar populations.

For example, Christensen et al. (2016) showed how the re-accretion of gas in the outskirts of MW-mass galaxies could introduce flows that have different angular momentum than the local reservoirs.

---

[5]We note here that even though our results do not completely rule out the possibility of a radial anisotropy at large radii within the 1σ uncertainty, the statistical confidence of tangential bias is comparable with what has been shown in the literature for dSphs and hence the comparison here is justified. Also, we would like to point out that such a tangential bias is not a result our imposed priors; we show in Fig. 4 the resulting prior on β_r given our input priors the model parameters, as the relevant model parameters all have uniform priors (β_z, κ, and DM halo parameters); our prior on β_r is also uniform and is allowed to go to highly radial values at large radii.

It is unclear if this would lead to preferential mixing of the newly formed stellar orbits in the tangential direction, or if it could apply in low-mass galaxies where there is evidence that a significant amount of the metals in the system may not have been retained or recycled (Kirby, Martin & Finlator 2011).

Latent dynamical heating of the stellar orbits in dwarf galaxies may be another mechanism to impart changes in the orbit distribution. Leaman et al. (2017) showed that the SFHs of Fornax, Sculptor, and WLM were largely consistent with the age–velocity dispersion being a result of dynamical cooling of the ISM as the gas fractions declined over time; however, low-level scattering of stars was still expected during epochs where the gas and newly formed stellar dispersion was $\lesssim 5$ km s^{-1}. Individual stars can scatter off overdensities (e.g. GMCs and spiral arms) in the molecular mid-plane of any galaxy.

GMC scattering is largely thought to result in both planar and vertical heating and isotropizes the stellar velocity ellipsoid, as the stellar discs are much thicker than the molecular gas layers. Scattering from spiral arms or bars is predominantly planar and so could increase the dispersion in the radial or tangential directions. However, dwarfs of this mass are much too thick and dynamically hot to form spiral arms. Bar formation has been invoked as an agent important in dwarf galaxy evolution; however, the simulations tend to predict either strongly radial (before bar buckling) or vertical (after bar buckling) anisotropies. Also, for dwarf galaxies of mass lower than WLM, bars are not really observed.

Other processes for which increasing evidence is being assembled are the aforementioned feedback-driven DM core creation and dwarf–dwarf mergers. The non-adiabatic change to the potential induced by the expulsion of gas in the centres of dwarf galaxies is suggested to result in preferentially larger orbit expansion for stars on circular orbits. If the response of these stars to the largely symmetric change to the potential is a net increase in their orbital radius, then could it be possible that the migrating stars enter final orbits with azimuthal velocities differing from the locally formed stars? El-Badry et al. (2017) studied the changes in anisotropy induced by potential fluctuations for dwarf galaxies of this mass, but even though they showed there could be variations, the anisotropy profiles were all significantly radial at all times and locations.

Mergers have been shown to temporarily induce tangential anisotropy in MW-mass galaxies, provided that the merging satellite remains coherent in the outskirts (Loebman et al. 2018). However, while there is increasing evidence for dwarf–dwarf mergers in the Local Group, and indeed Fornax (though not recent mergers; Leung et al. 2020), there is no concrete evidence presented in literature for mergers in the other two dwarf galaxies showing tangential anisotropy. A final speculative idea may be that the tangential anisotropy is a *consequence* of the prolate shape of the DM halo. This will be discussed in a follow-up paper.

While the exact cause of the anisotropy profile in WLM and its similarities to those seen in the dSphs is yet unclear, it is clear that the disparate environment posed by WLM offers an important constraint that simulations of isolated field dwarfs (and their potential transformation into dSphs) may want to reproduce.

WLM is an optimal candidate for the analysis we have presented here as both its mass and isolation are large enough that a significant dynamically cold gaseous component exists. It is observationally expensive to get stellar kinematics for such objects, but as we illustrate here, the improvement on the recovered DM properties is significant. Among other Local Group dIrrs, few have as well-defined H I rotation curves or existing stellar kinematic data sets. Irregular dwarfs with gas such as IC1613, NGC 6822, Sextans A/B, and Pegasus have more chaotic gas kinematic fields or non-optimal inclinations. However, Aquarius, Sagittarius dIrr, and VV124 may all be possible targets to repeat this type of joint stellar-gaseous dynamical modelling.

6 CONCLUSIONS

We performed JAMs on a discrete set of stellar kinematics, consisting of 180 stars, of an isolated dIrr galaxy WLM. The discrete stellar kinematics were obtained using FORS2 on VLT and DEIMOS on Keck, as reported by Leaman et al. (2009, 2012). Our models incorporated cold H I gas kinematics from Kepley et al. (2007) by introducing the measured circular velocities from H I, $V_{c, H I}$, as a prior to the total gravitational potential. We model the DM halo with the generalized NFW profile (Zhao 1996), characterized by the inner slope γ, the scale radius r_s, and the characteristic density ρ_s. We allow the flattening of the DM halo, q_{DM}, to be a free parameter in our models. The velocity anisotropy is described by $\beta_z = 1 - \sigma_z^2/\sigma_R^2$, which we take to be radially constant for our JAM models. We constrain our model parameters by employing Bayesian statistics. We show that all parameters are better constrained when including $V_{c, H I}$ as a prior in our model; the 1σ uncertainties of the parameters (β_z, q_{DM}, r_s, γ, and ρ_s) improve by 24 per cent, 15 per cent, 29 per cent, 48 per cent, and 54 per cent, respectively.

The DM halo is shown to be cored, with $\gamma = 0.34 \pm 0.12$. Such a cored DM halo is robust against variations in the DM flattening q_{DM} and different $M_\star$ values from the literature. Our inferred γ is also consistent with predictions by hydrodynamical CDM simulations, which suggest a relationship between the stellar-to-halo-mass ratio $M_\star/M_{halo}$ and the inner slope γ of the DM halo (Di Cintio et al. 2014). For our inferred value of $\gamma = 0.23 \pm 0.12$, when adopting $M_\star = 4.3 \times 10^7 \, M_\odot$, it is in excellent agreement with inner slope inferred by Di Cintio et al. (2014) of $\gamma = 0.25 \pm 0.16$.

We infer the radial anisotropy profile $\beta_r(r) = 1 - (\sigma_\phi^2 + \sigma_\theta^2)/2\sigma_r^2$ from our JAM models and found that the orbital structure of WLM is characterized by a mildly radially anisotropy core with $\beta_r(r = 0) = 0.32^{+0.03}_{-0.04}$ at the centre, which becomes increasingly tangential and reaches $\beta_r(r = 2 \, r_h) = -0.35^{+0.57}_{-0.90}$ at 2 half-light radii. This β_r profile is very similar to ones obtained from nearby dSph galaxies, such as Sculptor and Fornax. While it has been suggested that the tangential anisotropy in dSphs could be caused by preferential tidal stripping of stars on radial orbits, the isolated nature of WLM suggests that the tangential anisotropy in dwarf galaxies can be of primordial origin and may not be informative on the evolution between dIrrs to dSphs.

Our model shows that a prolate DM halo is preferred in WLM, albeit with relatively high uncertainties: $q_{DM} = 2.1^{+1.3}_{-0.9}$. The best-fitting value is in good agreement with the DM flattening found in ΛCDM cosmological simulations, both from DM-only or hydrodynamical simulations, both of which suggest a prolate DM halo with $q_{DM} \sim 2.0$ over the radii covered by our kinematic tracers ($\lesssim 5$ per cent r_{vir}) (Butsky et al. 2016). The derived prolate halo suggests challenges to MOND and some self-interacting DM models. These results are currently speculation, however, given the large uncertainties inferred for q_{DM}. Additionally, we show a $q_{DM} - \beta$ degeneracy that extends from $q_{DM} = 0.5$ to 4.0 in the 'Stars + Gas' models, which provides a window into a better-constrained q_{DM} if β can be constrained by other means such as proper motion measurements in future spectroscopic observations.

ACKNOWLEDGEMENTS

DATA AVAILABILITY

The stellar kinematic data underlying this article are available in the published papers (Leaman et al. 2009, 2012), or by request to the authors. The stellar photometry is presented in McConnachie et al. (2005) and requests for reduced photometry should be directed to those authors. The raw spectra are available via the ESO archive (http://archive.eso.org) and Keck archive (Brooks 2009). The H I observations from Kepley et al. (2007) are available in raw form from the VLA science archive (https://science.nrao.edu/facilities/vla/archive/index).

REFERENCES

Adams J. J. et al., 2014, ApJ, 789, 63
Battaglia G. et al., 2006, A&A, 459, 423
Battaglia G., Helmi A., Tolstoy E., Irwin M., Hill V., Jablonka P., 2008, ApJ, 681, L13
Battaglia G., Tolstoy E., Helmi A., Irwin M., Parisi P., Hill V., Jablonka P., 2011, MNRAS, 411, 1013
Battaglia G., Sollima A., Nipoti C., 2015, MNRAS, 454, 2401
Baumgardt H., Makino J., 2003, MNRAS, 340, 227
Beasley M. A., Trujillo I., 2016, ApJ, 830, 23
Binney J., Tremaine S., 1987, Galactic Dynamics. Princeton Univ. Press, Princeton, NJ
Breddels M. A., Helmi A., 2013, A&A, 558, A35
Breddels M. A., Helmi A., van den Bosch R. C. E., van de Ven G., Battaglia G., 2013, MNRAS, 433, 3173
Brook C. B., 2015, MNRAS, 454, 1719
Brooks A., 2009, Stellar Halo Formation in an Isolated Dwarf Galaxy. Keck Obs. Arch. DEIMOS
Brooks A. M., Zolotov A., 2014, ApJ, 786, 87
Butsky I. et al., 2016, MNRAS, 462, 663
Cappellari M., 2008, MNRAS, 390, 71
Christensen C. R., Davé R., Governato F., Pontzen A., Brooks A., Munshi F., Quinn T., Wadsley J., 2016, ApJ, 824, 57
Di Cintio A., Brook C. B., Dutton A. A., Macciò A. V., Stinson G. S., Knebe A., 2014, MNRAS, 441, 2986
Di Cintio A., Brook C. B., Dutton A. A., Macciò A. V., Obreja A., Dekel A., 2017, MNRAS, 466, L1
Dutton A. A., Macciò A. V., 2014, MNRAS, 441, 3359
El-Badry K., Wetzel A. R., Geha M., Quataert E., Hopkins P. F., Kereš D., Chan T. K., Faucher-Giguère C.-A., 2017, ApJ, 835, 193
Emsellem E., Monnet G., Bacon R., 1994, A&A, 285, 723
Errani R., Peñarrubia J., Walker M. G., 2018, MNRAS, 481, 5073
Fitts A. et al., 2019, MNRAS, 490, 962
Foreman-Mackey D., Hogg D. W., Lang D., Goodman J., 2013, PASP, 125, 306
Fritz T. K., Battaglia G., Pawlowski M. S., Kallivayalil N., van der Marel R., Sohn T. S., Brook C., Besla G., 2018, A&A, 619, A103
Fry A. B. et al., 2015, MNRAS, 452, 1468
González-Samaniego A., Bullock J. S., Boylan-Kolchin M., Fitts A., Elbert O. D., Hopkins P. F., Kereš D., Faucher-Giguère C.-A., 2017, MNRAS, 472, 4786
Hague P. R., Wilkinson M. I., 2013, MNRAS, 433, 2314
Hayashi K., Chiba M., 2012, ApJ, 755, 145
Helmi A., 2004, ApJ, 610, L97
Henon M., 1970, A&A, 9, 24
Hinz J. L., Rix H.-W., Bernstein G. M., 2001, AJ, 121, 683
Hunter D. A., Zahedy F., Bowsher E. C., Wilcots E. M., Kepley A. A., Gaal V., 2011, AJ, 142, 173
Hurley J. R., Shara M. M., 2012, MNRAS, 425, 2872
Iorio G., Fraternali F., Nipoti C., Di Teodoro E., Read J. I., Battaglia G., 2017, MNRAS, 466, 4159
Iorio G., Nipoti C., Battaglia G., Sollima A., 2019, MNRAS, 487, 5692
Jackson D. C., Skillman E. D., Gehrz R. D., Polomski E., Woodward C. E., 2007, ApJ, 656, 818
Jeans J. H., 1922, MNRAS, 82, 122
Kaplinghat M., Tulin S., Yu H.-B., 2016, Phys. Rev. Lett., 116, 041302
Katz H., Lelli F., McGaugh S. S., Di Cintio A., Brook C. B., Schombert J. M., 2017, MNRAS, 466, 1648
Kaufmann T., Wheeler C., Bullock J. S., 2007, MNRAS, 382, 1187
Keenan D. W., Innanen K. A., 1975, AJ, 80, 290
Kepley A. A., Wilcots E. M., Hunter D. A., Nordgren T., 2007, AJ, 133, 2242
Kereš D., Katz N., Weinberg D. H., Davé R., 2005, MNRAS, 363, 2
Khoperskov S. A., Moiseev A. V., Khoperskov A. V., Saburova A. S., 2014, MNRAS, 441, 2650
Kirby E. N., Martin C. L., Finlator K., 2011, ApJ, 742, L25
Kirby E. N., Bullock J. S., Boylan-Kolchin M., Kaplinghat M., Cohen J. G., 2014, MNRAS, 439, 1015
Klimentowski J., Łokas E. L., Kazantzidis S., Mayer L., Mamon G. A., 2009, MNRAS, 397, 2015
Kowalczyk K., del Pino A., Łokas E. L., Valluri M., 2019, MNRAS, 482, 5241
Leaman R., Cole A. A., Venn K. A., Tolstoy E., Irwin M. J., Szeifert T., Skillman E. D., McConnachie A. W., 2009, ApJ, 699, 1
Leaman R. et al., 2012, ApJ, 750, 33
Leaman R. et al., 2013, ApJ, 767, 131
Leaman R. et al., 2017, MNRAS, 472, 1879
Leauthaud A. et al., 2012, ApJ, 746, 95
Lelli F., Fraternali F., Sancisi R., 2010, A&A, 516, A11
Leung G. Y. C. et al., 2018, MNRAS, 477, 254
Leung G. Y. C., Leaman R., van de Ven G., Battaglia G., 2020, MNRAS, 493, 320
Li P., Lelli F., McGaugh S. S., Starkman N., Schombert J. M., 2019, MNRAS, 482, 5106
Loebman S. R. et al., 2018, ApJ, 853, 196
Łokas E. L., 2009, MNRAS, 394, L102
Macciò A. V., Dutton A. A., van den Bosch F. C., 2008, MNRAS, 391, 1940
Mashchenko S., Couchman H. M. P., Wadsley J., 2006, Nature, 442, 539
Massari D., Breddels M. A., Helmi A., Posti L., Brown A. G. A., Tolstoy E., 2018, Nat. Astron., 2, 156
McConnachie A. W., Irwin M. J., Ferguson A. M. N., Ibata R. A., Lewis G. F., Tanvir N., 2005, MNRAS, 356, 979
McGaugh S., Milgrom M., 2013, ApJ, 775, 139
Mayer L., 2010, Adv. Astron., 2010, 278434
Mayer L., Mastropietro C., Wadsley J., Stadel J., Moore B., 2006, MNRAS, 369, 1021
Melotte P. J., 1926, MNRAS, 86, 636
Merritt D., Hernquist L., 1991, ApJ, 376, 439
Milgrom M., 1983, ApJ, 270, 365
Mondal C., Subramaniam A., George K., 2018, AJ, 156, 109
Moster B. P., Somerville R. S., Maulbetsch C., van den Bosch F. C., Macciò A. V., Naab T., Oser L., 2010, ApJ, 710, 903

Navarro J. F., Eke V. R., Frenk C. S., 1996a, MNRAS, 283, L72

Navarro J. F., Frenk C. S., White S. D. M., 1996b, ApJ, 462, 563

O'Brien J. C., Freeman K. C., van der Kruit P. C., 2010, A&A, 515, A63

Oh S.-H., Brook C., Governato F., Brinks E., Mayer L., de Blok W. J. G., Brooks A., Walter F., 2011, AJ, 142, 24

Oñorbe J., Boylan-Kolchin M., Bullock J. S., Hopkins P. F., Kereš D., Faucher-Giguère C.-A., Quataert E., Murray N., 2015, MNRAS, 454, 2092

Peñarrubia J., Pontzen A., Walker M. G., Koposov S. E., 2012, ApJ, 759, L42

Peter A. H. G., Rocha M., Bullock J. S., Kaplinghat M., 2013, MNRAS, 430, 105

Peters S. P. C., van der Kruit P. C., Allen R. J., Freeman K. C., 2017a, MNRAS, 464, 32

Peters S. P. C., van der Kruit P. C., Allen R. J., Freeman K. C., 2017b, MNRAS, 464, 65

Pontzen A., Governato F., 2012, MNRAS, 421, 3464

Raha N., Sellwood J. A., James R. A., Kahn F. D., 1991, Nature, 352, 411

Read J. I., Gilmore G., 2005, MNRAS, 356, 107

Read J. I., Steger P., 2017, MNRAS, 471, 4541

Read J. I., Wilkinson M. I., Evans N. W., Gilmore G., Kleyna J. T., 2006, MNRAS, 367, 387

Read J. I., Agertz O., Collins M. L. M., 2016, MNRAS, 459, 2573

Read J. I., Walker M. G., Steger P., 2019, MNRAS, 484, 1401

Robles V. H. et al., 2017, MNRAS, 472, 2945

Sameie O., Creasey P., Yu H.-B., Sales L. V., Vogelsberger M., Zavala J., 2018, MNRAS, 479, 359

Satoh C., 1980, PASJ, 32, 41

Sawala T., Frenk C. S., Crain R. A., Jenkins A., Schaye J., Theuns T., Zavala J., 2013, MNRAS, 431, 1366

Schive H.-Y., Liao M.-H., Woo T.-P., Wong S.-K., Chiueh T., Broadhurst T., Hwang W.-Y. P., 2014, Phys. Rev. Lett., 113, 261302

Schroyen J., de Rijcke S., Valcke S., Cloet-Osselaer A., Dejonghe H., 2011, MNRAS, 416, 601

Shen S., Madau P., Conroy C., Governato F., Mayer L., 2014, ApJ, 792, 99

Swaters R. A., Sancisi R., van Albada T. S., van der Hulst J. M., 2011, ApJ, 729, 118

Tatton B., Cioni M. R., Irwin M., 2011, in Kerschbaum F., Lebzelter T., Wing R. F., eds, ASP Conf. Ser. Vol. 445, Why Galaxies Care about AGB Stars II: Shining Examples and Common Inhabitants. Astron. Soc. Pac., San Francisco, p. 547

Teyssier R., Pontzen A., Dubois Y., Read J. I., 2013, MNRAS, 429, 3068

van Albada T. S., 1982, MNRAS, 201, 939

Vogelsberger M., Zavala J., Loeb A., 2012, MNRAS, 423, 3740

Vogelsberger M., Zavala J., Simpson C., Jenkins A., 2014, MNRAS, 444, 3684

Vogelsberger M., Zavala J., Cyr-Racine F.-Y., Pfrommer C., Bringmann T., Sigurdson K., 2016, MNRAS, 460, 1399

Vogelsberger M., Zavala J., Schutz K., Slatyer T. R., 2019, MNRAS, 484, 5437

Vorontsov-Velyaminov B. A., 1959, Atlas and Catalog of Interacting Galaxies. Moscow State Univ., Moscow

Walker M. G., Peñarrubia J., 2011, ApJ, 742, 20

Weisz D. R., Dolphin A. E., Skillman E. D., Holtzman J., Gilbert K. M., Dalcanton J. J., Williams B. F., 2014, ApJ, 789, 147

Wheeler C. et al., 2017, MNRAS, 465, 2420

Whiting A. B., Hau G. K. T., Irwin M., 1999, AJ, 118, 2767

Wolf M., 1910, Astron. Nachr., 183, 137

Wolf J., 2010, Highlights Astron., 15, 79

Zhao H., 1996, MNRAS, 278, 488

Zhu L., van de Ven G., Watkins L. L., Posti L., 2016, MNRAS, 463, 1117

Zolotov A. et al., 2012, ApJ, 761, 71

APPENDIX A: DEPENDENCE ON THE CHOSEN DENSITY PROFILE OF KINEMATIC TRACER

Here we investigate the effects of the chosen input surface density profile of the kinematic tracer. In the main text, we have chosen the RGB star counts, fitted with an exponential profile excluding the inner

region ($\sim$5 arcmin) of the galaxy that might be affected by crowding, to represent the density profile of the kinematic tracer, as shown in Fig. 2 and the corresponding MGEs listed in Table 3. We label this profile as 'Rexp'. We then rerun the discrete Jeans models on four other density profiles: (1) the uncorrected RGB star counts 'R', (2) total star counts with again exponentially corrected profile 'Aexp', (3) uncorrected total star counts 'A', and (4) *I*-band photometry, 'I'; the fitted MGE parameters of (1)–(3) are shown in Tables A1–A3, and (4) in Table 2 in the main text. The fitting of the MGEs to the star-count profiles from (1) to (3) is shown in Fig. A1. The best-fitting and 1σ uncertainties of the MCMC parameters constrained from the discrete Jeans model made with each of the profiles are shown in Fig. A2 in black for the 'Stars only' case and in red for the 'Stars + Gas' case.

Under all the tested density profiles, a cored DM halo with $\gamma <$ 0.5 is recovered. Furthermore, except for the models ran with *I*-band photometry as the kinematic tracer's density, a prolate DM halo with $q_{DM} \gtrsim 2$ is preferred. Such a discrepancy is likely caused by the spatial scale at which the density profiles drop off. Its integrated-light nature causes the *I*-band photometry to drop off at a smaller scale than the other density profiles, which are by nature discrete. The *I*-band photometry is also shown to have a much smaller spatial coverage than our kinematic tracers (see Figs 1c and d). The derived
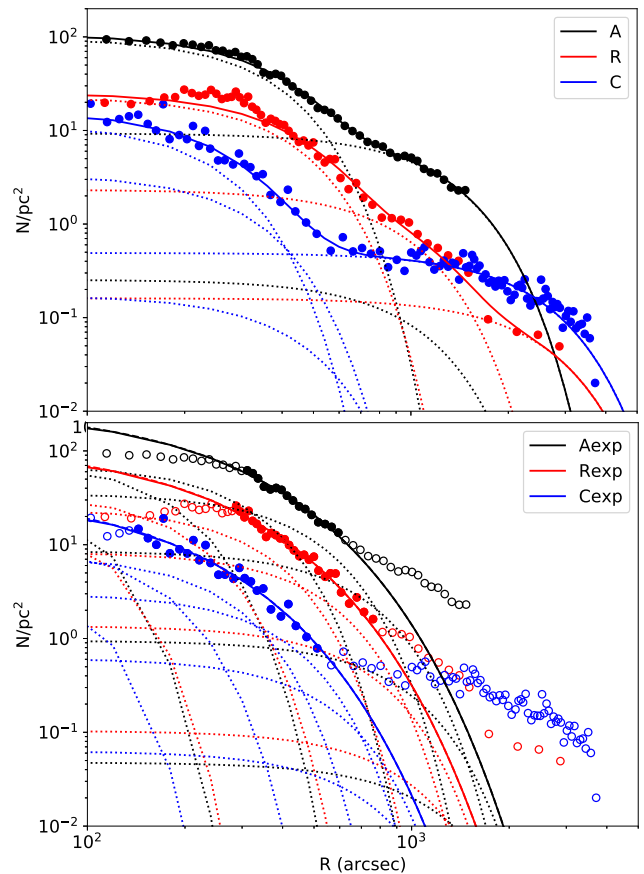

Figure A1. Fitted MGEs to RGB stars (red) and C stars (blue). Solid circles show the observed radial profile of the number density of the respective star type. The solid lines show the best-fitting MGEs and the dotted lines show the individual MGEs. The MGEs fitted from RGB stars are used for both the middle-aged and old populations and the ones from C stars are used for the young population.
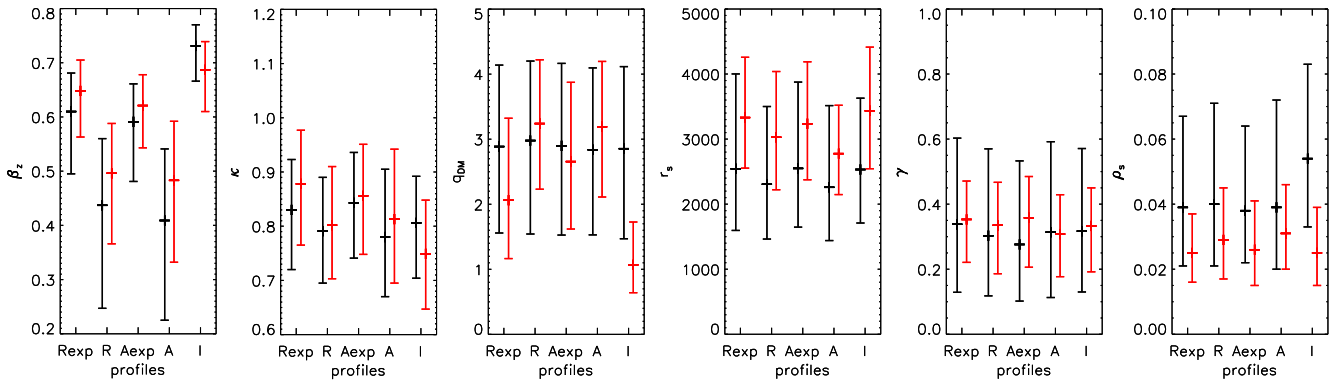
Figure A2. Constrained parameters from discrete Jeans models using different density profiles as representation of the kinematic tracer's density profile, with black representing the results from the 'Stars only' and red representing the results from the 'Stars + Gas' models. The y-axis of each panel shows the constraints of a free parameter in the model, from left to right: velocity anisotropy β_z, κ, DM halo flattening q_{DM}, DM halo scale radius r_s, inner slope of the DM density profile γ, and the characteristic density ρ_s. The x-axis corresponds to the five density profiles that we tested: 'Rexp': RGB star counts fitted with an exponential profile excluding the inner region that might be affected by crowding; 'R': RGB star counts; 'Aexp': total star counts fitted with an exponential profile excluding the inner region; 'A': total star counts; and 'I': *I*-band photometry.

Table A1. MGE of the RGB star counts ('R'), normalized to a total stellar mass of $M_\star = 1.1 \times 10^7\,M_\odot$.

$I_{0,\star}$ ($M_\odot$ pc^{-2})	$\sigma_\star$ (arcsec)	$q_\star$
1.318	278.772	0.422
0.134	622.446	0.422
9.280×10^{-3}	1660.687	0.422

Table A2. MGE of the exponentially corrected total star counts ('Aexp'), normalized to a total stellar mass of $M_\star = 1.1 \times 10^7\,M_\odot$.

$I_{0,\star}$ ($M_\odot$ pc^{-2})	$\sigma_\star$ (arcsec)	$q_\star$
1.035	58.378	0.422
1.389	120.767	0.422
1.218	211.198	0.422
0.603	326.504	0.422
0.147	460.855	0.422
1.621×10^{-2}	607.298	0.422
8.153×10^{-4}	759.947	0.422
1.838×10^{-5}	918.728	0.422
1.156×10^{-7}	1100.052	0.422

Table A3. MGE of the total star counts ('A'), normalized to a total stellar mass of $M_\star = 1.1 \times 10^7\,M_\odot$.

$I_{0,\star}$ ($M_\odot$ pc^{-2})	$\sigma_\star$ (arcsec)	$q_\star$
1.372	249.495	0.422
3.581×10^{-2}	668.103	0.422
0.131	842.278	0.422

β_z from the model using 'I' as the tracer density profile is also slightly higher than those derived using the other profiles' kinematics.

APPENDIX B: COMPARISON TO SPHERICAL JEANS MODEL

Here we compare the dynamical and DM parameters as constrained from our JAM model with spherical Jeans model that are commonly used for dwarf galaxies. We use radially binned mean velocity

(V_{mean}) and velocity dispersion (σ) of our discrete kinematics and the spherical Jeans equation, implemented using the publicly available code by Cappellari (2008). The V_{mean} and σ profiles are shown in dashed and dotted lines, respectively, on the top panel of Fig. B1, and the corresponding observed second moment $V_{RMS} = \sqrt{V_{mean}^2 + \sigma^2}$ and the error bars are plotted in solid lines. The gaseous and stellar MGEs used are the same as the ones listed in Tables 1 and 2, but with $q = 1$ and renormalized to the total stellar and gaseous masses, respectively. The DM haloes are parametrized with a gNFW profile.

We again use MCMC to fit the spherical Jeans models to the data, adopting the 'Rexp' as the density profile of the kinematic tracer with $q = 1$ for all MGEs. The number of walkers, steps, and burn-in are the same as the ones we adopt in the axisymmetric case. Since we are using binned data, there is no need to specify κ. The relevant velocity anisotropy in the Jeans model is $\beta_\phi = \beta_\theta = 1 - \sigma_\phi^2/\sigma_r^2$.[6] The free parameters are therefore $M_\star$, β_ϕ, r_s, γ, and ρ_s; we assume β_ϕ to be constant. We again perform two sets of models, one with constraints from $V_{c,\,HI}$ and one without. The constrained parameters are plotted in Fig. B2, in black are the models from the 'Stars only' runs, and in red the models from the 'Stars + Gas' runs.

Just like in the axisymmetric models, the DM parameters are much better constrained when we include $V_{c,\,HI}$ as a constraint on the total gravitational potential. The result from the axisymmetric model of a cored DM halo remains robust under the spherical Jeans model, which derives a γ of $0.37^{+0.11}_{-0.14}$ in the 'Stars + Gas' case. Although β_ϕ is poorly constrained in both the 'Stars only' and 'Stars + Gas' cases, it is confirmed here that the stars have a tangential velocity anisotropy, with $\beta_\phi(= \beta_r)$ being highly negative ($-1.67^{+1.03}_{-1.66}$ in the 'Stars + Gas' case), just as we find from our discrete JAM models. There is no significant improvement in the constraint on stellar velocity anisotropy by including $V_{c,\,HI}$, reaffirming our interpretation that the improvement of the constraint of β_z in the axisymmetric models when including $V_{c,\,HI}$ comes mainly from breaking the $q_{DM} - \beta$ degeneracy.

---

[6]Under spherical symmetry, this would correspond to the radial anisotropy parameter defined in Section 4.2: $\beta_r = \beta_\phi = \beta_\theta$.
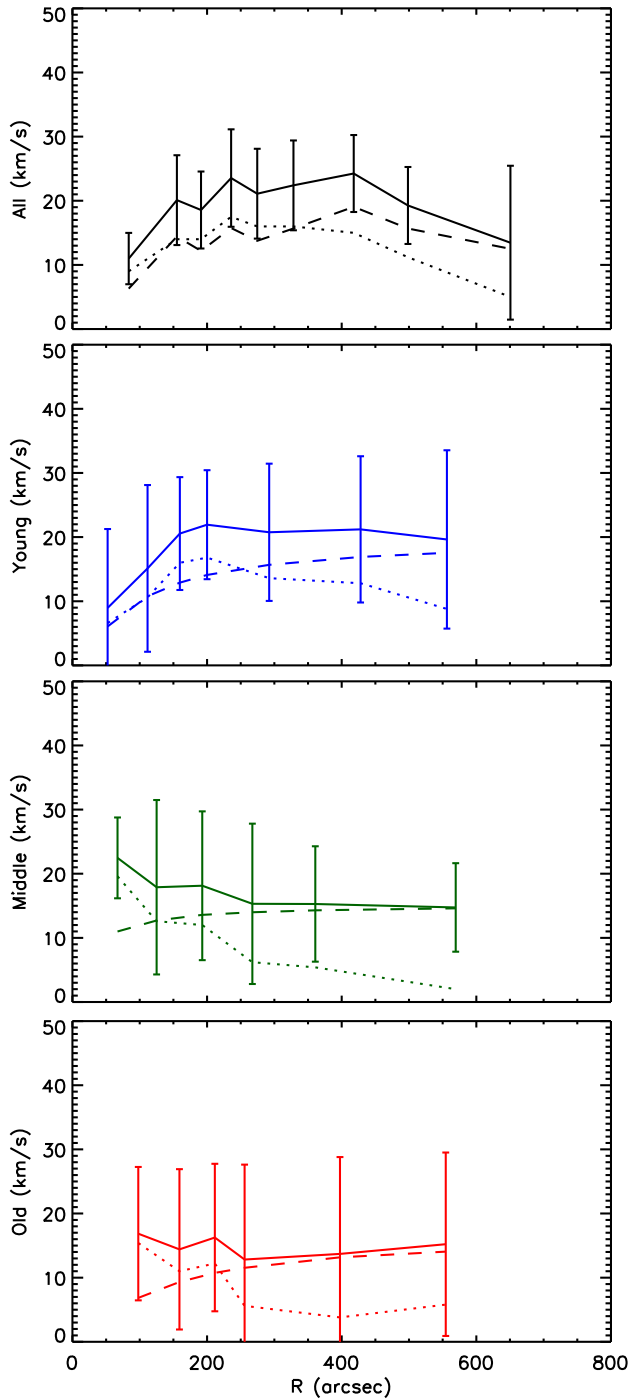
Figure B1. Binned stellar mean velocity and velocity dispersion. Top panel: The binned mean velocity V_{mean} (dashed line) and velocity dispersion σ (dotted line) of all the stars in our discrete sample. The solid line shows the second velocity moment $V_{RMS} = \sqrt{V_{mean}^2 + \sigma^2}$ as an input to the Jeans model. The binned V_{mean}, σ, and V_{RMS} profiles of the young, middle, and old populations are shown in blue, green, and red, respectively.

B1 Multipopulation spherical Jeans models

It has been shown that the stellar velocity anisotropy depends on their metallicity, and by separating the stars into a metal-rich population and a metal-poor population one can obtain a better constraint on the velocity anisotropy (e.g. Battaglia et al. 2006, 2011). We test here
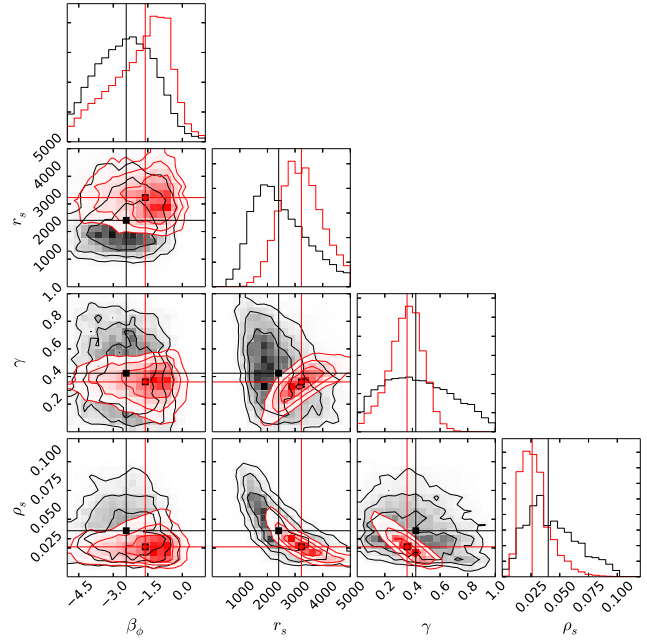

Figure B2. Marginalized parameters from the spherical Jeans models, adopting the 'Rexp' profile as the surface density profile of the kinematic tracer: the dynamical parameters β_ϕ, and the DM parameters r_s, γ, and ρ_s. Black contours show the marginalized parameter values with Jeans models performed only on stellar kinematics. Red contours show the ones constrained by using V_c derived from H I kinematics as a prior.

Table B1. MGE of the exponentially corrected C star counts ('Cexp'), normalized to a total stellar mass of $M_\star = 1.1 \times 10^7 \, \mathrm{M_\odot}$.

$I_{0,\star}$ ($\mathrm{M_\odot \, pc^{-2}}$)	$\sigma_\star$ (arcsec)	$q_\star$
2.426	54.426	0.422
2.801	107.155	0.422
1.980	178.505	0.422
0.774	263.719	0.422
0.157	358.019	0.422
1.611×10^{-1}	458.012	0.422
8.175×10^{-4}	561.771	0.422
1.982×10^{-5}	668.999	0.422
1.986×10^{-7}	782.365	0.422
4.608×10^{-10}	912.600	0.422

whether we can obtain an even better constraint by adding the $V_{c, \mathrm{H I}}$ constraint to the multipopulation models.

Leaman et al. (2009) have shown that the metal-rich and metal-poor populations in WLM share similar spatial distributions. Here we instead separate the stars into three populations by their ages and characterize their spatial distributions with density profiles from C and RGB stars. The C star profile is used for the young population (<2 Gyr), and the RGB star profile is used for the middle (2–10 Gyr) and old populations (>10 Gyr). We adopt here the 'Rexp' and 'Cexp' (an exponential fit to the C star profile neglecting the inner 2 arcmin for which the fitted MGE parameters are listed in Table B1) profiles that avoid issues with overcrowding of stars at the centre of the galaxy. We then fit MGEs to the derived exponential profiles. The MGE fittings are shown in Fig. A1 in red for the RGB stars and blue for the C stars. The V_{mean}, σ, and V_{RMS} for the young, middle, and old populations are shown in Fig. B1 in blue, green, and red, respectively. The free parameters here are the velocity anisotropies

for the young, middle, and old age populations: $\beta_{\phi,y}$, $\beta_{\phi,m}$, and $\beta_{\phi,o}$, and the DM parameters γ, r_s, and ρ_s.

The constrained parameters are plotted in Fig. B3, again with black showing the 'Stars only' case and red the 'Stars + Gas' case. Compared to the single-population models, only the middle-aged population shows a better constrained $\beta_{\phi,m}$ of $0.13^{+0.48}_{-1.19}$, while both the young- and old-aged populations show similar β_ϕ of $\beta_{\phi,y} = -1.16^{+1.06}_{-1.82}$ and $\beta_{\phi,o} = -1.15^{+1.34}_{-1.81}$. The derived inner slope of the DM halo in the 'Stars + Gas' case is 0.29 ± 0.12, again reaffirming the cored density profile.
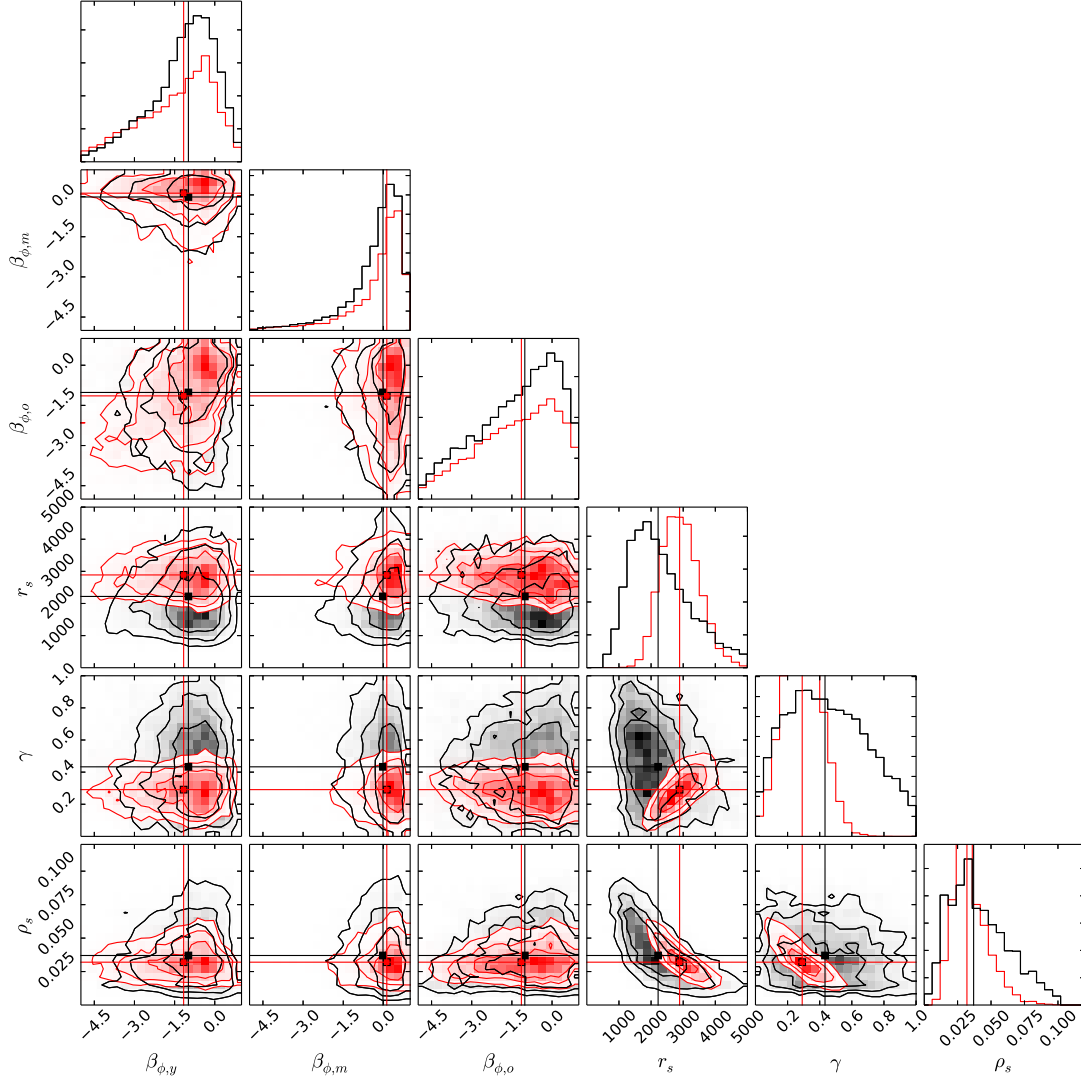

Figure B3. Marginalized parameters from the spherical Jeans models: the velocity anisotropy for the young ($\beta_{\phi,y}$), middle-aged ($\beta_{\phi,m}$), and old population ($\beta_{\phi,o}$), and the DM parameters r_s, γ, and ρ_s. Black contours show the marginalized parameter values with Jeans models performed on only stellar kinematics. Red contours show the ones constrained by using V_c derived from H I kinematics as a prior.

This paper has been typeset from a TEX/LATEX file prepared by the author.